NAVAL POSTGRADUATE SCHOOL

MONTEREY, CALIFORNIA

THESIS

GaN LIGHT EMISSION FOR CONTROL SYSTEM FEEDBACK

by

Johnathan L. Williams

December 2020

Thesis Advisor:	Todd R. Weatherford
Co-Advisor:	Keith Corzine, UC Santa Cruz
Second Reader:	Matthew A. Porter

THIS PAGE INTENTIONALLY LEFT BLANK

REPORT DOCUMENTATION PAGE			*Form Approved OMB No. 0704-0188*

1. AGENCY USE ONLY *(Leave blank)*	**2. REPORT DATE** December 2020	**3. REPORT TYPE AND DATES COVERED** Master's thesis

4. TITLE AND SUBTITLE GaN LIGHT EMISSION FOR CONTROL SYSTEM FEEDBACK	**5. FUNDING NUMBERS** RENU3
6. AUTHOR(S) Johnathan L. Williams	
7. PERFORMING ORGANIZATION NAME(S) AND ADDRESS(ES) Naval Postgraduate School Monterey, CA 93943-5000	**8. PERFORMING ORGANIZATION REPORT NUMBER**
9. SPONSORING / MONITORING AGENCY NAME(S) AND ADDRESS(ES) Office of Naval Research; Arlington, VA 22217	**10. SPONSORING / MONITORING AGENCY REPORT NUMBER**

11. SUPPLEMENTARY NOTES The views expressed in this thesis are those of the author and do not reflect the official policy or position of the Department of Defense or the U.S. Government.

12a. DISTRIBUTION / AVAILABILITY STATEMENT Approved for public release. Distribution is unlimited.	**12b. DISTRIBUTION CODE** A

13. ABSTRACT (maximum 200 words)

This work explores previous research showing the correlation of light emission to current and temperature in a gallium nitride (GaN) vertical diode to predict current within a power converter circuit. Use of light emissions to measure current would offer an improvement over present sensors, since light would not be affected by the EMI found in most switched power converters. Matrices of the light emissions at 370, 380, 390, 400, 440, and 550 nm wavelengths over a range of 0.2 A to 4 A and 20 °C to 110 °C were used to develop best-fit polynomials for each matrix. Two of these polynomials can then be utilized to derive a unique solution of current and temperature based on the light output at the distinct wavelengths. Lock-in amplifiers allowed the amplification of weak light signals without gain bandwidth product limitations. Future efforts will be to duplicate the lock-in amplifier as well as the current and temperature prediction with use of a microcontroller.

14. SUBJECT TERMS gallium nitride, GaN, light emissions, power control system feedback	**15. NUMBER OF PAGES** 93
	16. PRICE CODE

17. SECURITY CLASSIFICATION OF REPORT	**18. SECURITY CLASSIFICATION OF THIS PAGE**	**19. SECURITY CLASSIFICATION OF ABSTRACT**	**20. LIMITATION OF ABSTRACT**
Unclassified	Unclassified	Unclassified	UU

NSN 7540-01-280-5500 Standard Form 298 (Rev. 2-89) Prescribed by ANSI Std. 239-18

THIS PAGE INTENTIONALLY LEFT BLANK

Approved for public release. Distribution is unlimited.

GaN LIGHT EMISSION FOR CONTROL SYSTEM FEEDBACK

Johnathan L. Williams
Lieutenant, United States Navy
BSAST, Thomas A Edison State College, 2013

Submitted in partial fulfillment of the
requirements for the degree of

MASTER OF SCIENCE IN ELECTRICAL ENGINEERING

from the

NAVAL POSTGRADUATE SCHOOL
December 2020

Approved by: Todd R. Weatherford
Advisor

Keith Corzine
Co-Advisor

Matthew A. Porter
Second Reader

Douglas J. Fouts
Chair, Department of Electrical and Computer Engineering

THIS PAGE INTENTIONALLY LEFT BLANK

ABSTRACT

This work explores previous research showing the correlation of light emission to current and temperature in a gallium nitride (GaN) vertical diode to predict current within a power converter circuit. Use of light emissions to measure current would offer an improvement over present sensors, since light would not be affected by the EMI found in most switched power converters. Matrices of the light emissions at 370, 380, 390, 400, 440, and 550 nm wavelengths over a range of 0.2 A to 4 A and 20 °C to 110 °C were used to develop best-fit polynomials for each matrix. Two of these polynomials can then be utilized to derive a unique solution of current and temperature based on the light output at the distinct wavelengths. Lock-in amplifiers allowed the amplification of weak light signals without gain bandwidth product limitations. Future efforts will be to duplicate the lock-in amplifier as well as the current and temperature prediction with use of a microcontroller.

THIS PAGE INTENTIONALLY LEFT BLANK

TABLE OF CONTENTS

LIST OF FIGURES

LIST OF TABLES

THIS PAGE INTENTIONALLY LEFT BLANK

LIST OF ACRONYMS AND ABBREVIATIONS

A	amps
A2D	analog to digital
AlGaAs	aluminum, gallium, arsenide
AlGaInP	aluminum, gallium, indium, phosphate
AlInGaN	aluminum, indium, gallium, nitrogen
C	carbon
C_{Ga}	carbon substitution for gallium
D2A	precursor digital to analog
DAP	donor-acceptor-pair
DSP	digital signal processing
DUT	device under test
EMI	electromagnetic interference
eV	electron volts
FET	field effect transistor
FPGA	field programmable gate array
FOM	figure of merit
GaN	gallium nitride
HEMT	high electron mobility transistors
LED	light emitting diode
LNA	low noise amplifier
MCU	microcontroller unit
Mg	magnesium
mm	millimeter
MOCVD	metal organic chemical vapor deposition
nm	nanometer
NPS	Naval Postgraduate School
NRL	Naval Research Laboratory
PSD	phase sensitive detection
PN	positive doped/negative doped
PWM	pulse width modulation

X1A	direct excitonic light emission
X1A-LO	phonon (LO) assisted excitonic light emission
RLC	resistive, inductive, and capacitive
s	seconds
Si	silicon
SiC	silicon carbide
TEC	thermoelectric cooler
TI	Texas Instruments
V	volts
VCCS	voltage controlled current source
W	watt

ACKNOWLEDGMENTS

Matt, despite all your quirks, I would not be submitting this work without you. From the bottom of my heart—thank you for everything.

Professor Weatherford, thank you for making this happen. I truly have valued everything associated with this research and I am grateful for your willingness to help me get through this.

Professor Corzine, your patience and consistency are another instrumental part of this work, and my sanity, for which I cannot say thank you enough. Looking back, I regret we did not start getting together sooner and feel that it could have resulted in so much more progress.

Finally, I want to thank my family and the writing center for all their support and for gracefully putting up with and getting me though all my shortcomings.

THIS PAGE INTENTIONALLY LEFT BLANK

I. INTRODUCTION

The need for power electronic devices that can operate efficiently at higher frequencies and powers continues to grow in nearly every facet of our society today. Whether in cell phones, electric cars, healthcare equipment, power distribution grids, or military systems, the growth creates a need for better, faster, and more capable electronic systems which will continue to increase for the foreseeable future. High-efficiency, power-dense systems require highly regulated signal and power circuits to achieve these objectives with greater precision and endurance. The Navy stealth destroyer is just one example. The U.S. Navy is seeking to use an integrated electrical power system in the DDG 1000 that would feed and monitor an electrical propulsion system, directed energy and laser weapons, and the latest navigation, combat and fire suppression systems [1]. Satellite communication systems are another field with substantial projected growth due to the onset of 5G data requirements and with the need of maximum optimization of capability, size, and the ability to operate within the harshest of environments [2]. Other commercial and industrial applications, in general, have been no different with the need of equipment to perform tasks with similar growth in speed and robustness. These needs have spurred continued research into new materials with properties exceeding those of silicon (Si) as well as the design of associated power systems of these electronic devices which require monitoring of their output circuits in order to respond to changing load demands. A power system must often meet the same rigorous standards of precision and consistency as the equipment it supplies. However, popular sensors used in the monitoring of these systems are susceptible to the electromagnetic interference (EMI) that is common within switched power systems—thus creating a need to monitor these power system circuits via a more robust method.

As the search for better materials to use in electronics continues, power electronics manufacturers have increasingly looked into the use of wide bandgap semiconductors for their increased durability. The field of wide bandgap semiconductors consists of several materials to include silicon carbide (SiC) and diamond. This field also includes gallium nitride (GaN), which has been used as an alloy in light emitting diodes for some time as its

direct bandgap structure yields a high rate of visible photonic emissions at currents of less than 1A [3], [4]. Use of GaN in power applications, however, was previously limited due to challenges in growing high-quality bulk substrates, but now has been addressed by multiple crystalline growth methods [5]–[7]. Today, GaN is increasingly being used within power devices with breakdown/blocking voltages demonstrated as high as 5.0 kV, turn-on voltages as low as 0.39 V, and a Baliga's figure of merit (which defines conduction loss in a field effect transistor) that exceeds silicon carbide (SiC) and Si [8]–[11].

A. RESEARCH OBJECTIVE

This thesis explores the use of photonic emissions from a forward-biased GaN PN junction as a means of measuring current and temperature of a GaN flyback diode in a switched power circuit. Such a capacity would eliminate the need for current and temperature sensors which are vulnerable to electromagnetic interference (EMI). Furthermore, this improved method of predicting current via light emission of the diode would allow for improved monitoring and response of power system control, particularly in a switched power system, such as a buck converter, where a wideband semiconductor like GaN would typically be used.

B. RELATED WORK

III-Nitride alloys (and specifically gallium nitride) are a common component of LEDs and an increasingly popular material used in power electronic and military applications [3], [12]. While uses of this material differ based on its application, previous research suggests that the photonic emissions (in the form of light) may be used to provide data about the bias current flowing within bipolar direct bandgap devices in addition to temperature and, possibly, indications of device degradation [13], [14]. One goal is to use these photonic emissions to provide an alternative to the use of Hall-effect sensors for current monitoring and thereby negating EMI effects. Noting previous research, Tosi et al. have shown light emission may be used to evaluate fabrication errors in semiconductors [15]. Furthermore, Khanna et al. have observed degradation in the intensity of light emissions at dominant wavelengths from GaAs after nuclear radiation and concluded that predictions of damage to the material were possible from the changes in the emission

intensity [14]. These two findings support the monitoring of photonic emissions for trend analysis and suggest it may also be possible to warn of device degradation before it fails. Also of interest, since this research will be based on the photonic emissions of GaN, is information suggesting that a system designed for use of GaN photonic emissions may be compatible with other wide bandgap materials. The findings of Ceccarelli et al. demonstrated the use of light emission to predict temperature in a high voltage SiC metal oxide semiconductor field effect transistor (MOSFET) [16]. Kalker et al. reported a similar finding, but were also able to predict current using electroluminescence with the use of a neuro network while Winkler et al. also made current and temperature predictions of SiC power MOSFETs using data from prerecorded silicon photo multiplier detections [17]–[19]. These findings support and have interesting parallels with research conducted by a joint venture between the University of Santa Cruz and Naval Postgraduate School (NPS) into electroluminescence of GaN. In her 2019 thesis, Maeve Broeg reported the intensity of photonic emissions varied with both current and temperature [13]. Results from this testing also identified distinct wavelengths emitted by a GaN diode which shifted in intensity and wavelength due to temperature and current changes.

C. THESIS ORGANIZATION

This thesis is laid out as follows. Chapter II will cover properties of wide bandgap semiconductors in general, followed by those of GaN in particular, and then provide a general overview of expected power electronic applications. Experimental system design with optical filter selection and calibration data collection is explained in Chapter III with testing of the system against various waveforms detailed in Chapter IV. Chapter V contains the use of microcontrollers to maximize the ability of the experimental system and feasibility for use in commercial and industrial applications. Finally, conclusions and opportunities for further work are provided in Chapter VI.

THIS PAGE INTENTIONALLY LEFT BLANK

II. BACKGROUND

This chapter introduces gallium nitride in its general characterization as a wideband semiconductor and broadly covers why these materials are desirable for electrics in terms of size, durability, and performance, especially in the use of power electronics. Specific properties of GaN are then discussed—validating its use in current and for future applications followed by an explanation of why light is observed from GaN devices. Finally, details of a commonly used power converter are explored along with the use of Hall-effect sensors in the control of switched power converters.

A. PROPERTIES OF GALLIUM NITRIDE

As mentioned in Chapter I, GaN is both a direct bandgap material and a wide bandgap semiconductor, and it is for the combination of these two properties that GaN was chosen for this investigation. Because photonic emissions (light) from devices already present in circuits can provide indications of device degradation, and because these emissions are not affected by EMI, it seems logical to explore the exploitation of photonic emissions as a monitoring means for control of power systems. Hence, it is necessary to look deeper into how these photonic emissions are created and how a direct bandgap contributes to this light-emitting phenomenon of recombination, in addition to the value of wide-bandgap semiconductors and how GaN ranks within this field before exploring its use within a power circuit.

1. Wideband Semiconductors and GaN

A semiconductor, requiring greater than 2.0 electron volts (eV) of energy to move an electron from the valence band of the atom into the conduction band, is referred to as a wide-bandgap or wideband material [12]. Structurally, these materials are known for their crystalline structure with close lattice spacing and the inclusion of atoms from the upper right-hand side of the periodic table that form a combined total of eight valence electrons. Elements such as nitrogen in group V have high electronegativity, resulting in high bond strength in compounds with group III elements. These bonds result in a much higher energy to move the electrons into the conduction band. Consequently, an electron falling from the

conduction band back into the valence band from these elements yields higher energy photons required for higher frequency devices [12]. The tightly bonded crystalline structure yields a material relatively inert and it is this close bond that also helps in the efficient propagation if thermal phonons (heat) resulting the ability to transfer heat quickly and higher operational temperatures, as shown in Table 1 [20].

Table 1. Wide bandgap semiconductor properties. Adapted from [21].

Semiconductor Material	Bandgap (eV) Direct, D Indirect, I	Electron Mobility $\mu(cm^2/V_S)$	Hole Mobility $\mu(cm^2/V_S)$	Density (g/cm^3)	Critical of Breakdown Field E_c (V/cm)	Themal Conductivity σ_f(W/m*K)	Coefficient of Thermal Expansion (ppm/K)
InSb	0.17, D	77000	850	5.77	1000	18	5.37
InAs	0.354, D	44000	500	5.68	40000	27	4.52
GaSb	0.726, D	3000	1000	5.61	50000	32	7.75
InP	1.344, D	5400	200	4.81	500000	68	4.6
GaAs	1.424, D	8500	400	5.32	400000	55	5.73
GaN	3.44, D	900	10	6.1	3000000	110	5.4-7.2
Ge	0.661, I	3900	1900	5.32	100000	58	5.9
Si	1.12, I	1400	450	2.33	300000	130	2.6
GaP	2.26, I	250	150	4.14	1000000	110	4.65
SiC (3C,β)	2.36, I	300-900	30-Oct	3.17	1300000	700	2.77
SiC (6H,α)	2.86, I	330-400	75	3.21	2400000	700	5.12
SiC (4H,α)	3.25, I	700			3180000	700	5.12
C (diamond)	5.46-5.6, I	2200	1800	3.52	5700000	600-2000	0.8

Of note, GaN has a thermal conductivity significantly lower than SiC and is roughly equal to Si. However, the higher mobility rate and breakdown field of GaN when compared to SiC will, theoretically, generate less heat and can withstand greater temperatures. Thermal conductivity and mobility are closely linked to resistance and Baliga's figure of merit (FOM). This relationship is best explained by using an ideal drift region one dimensional Schottky diode, as shown in Figure 1, which by definition contains a uniformly doped drift region and a triangular electric field distribution [22].

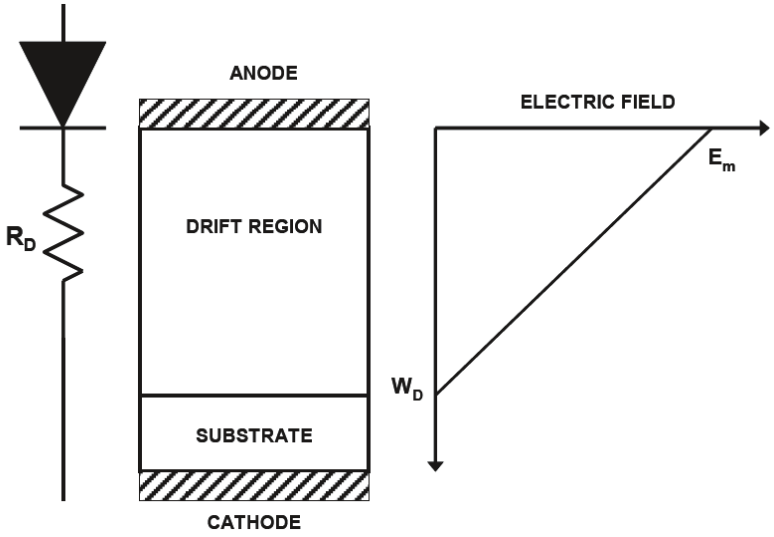

Figure 1. Schematic and depiction of an ideal Schottky diode and the electrical field distribution. Source: [22].

In such a device, the specific resistance (R_{onsp}) is a function of the width of the drift region (W_D), the charge of an electron (q), the mobility of the material used (μ_n), and the doping of the material (N_D), as shown in Equation 1.

$$R_{onsp}\left[\Omega \cdot cm^2\right] = \frac{W_D}{q\mu_n N_D} \tag{1}$$

By restating the drift zone width and doping in terms of the critical electrical field (E_c) and breakdown voltage (BV) (Equations 2 and 3) with ε_s representing the dielectric constant, Equation 1 can then be written in terms of its material specific properties (Equation 4).

$$W_D = \frac{2BV}{E_c} \tag{2}$$

$$N_D = \frac{\varepsilon_s \mathrm{E}_c^2}{2qBV} \tag{3}$$

$$R_{on} = \frac{4BV^2}{\varepsilon_s \mu_n E_c^3} \tag{4}$$

Baliga's FOM is the denominator of Equation 4 and it is through this FOM that the properties of GaN are truly desirable having both a high mobility and reasonably large electric field, as shown in Figure 2.

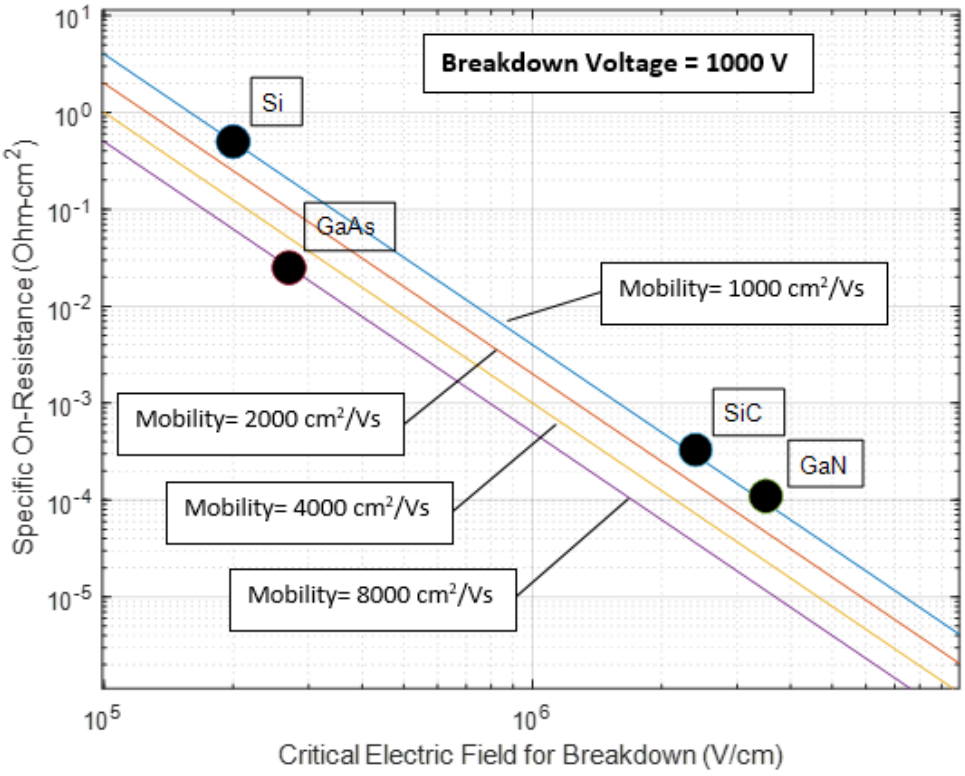

This chart shows specific on resistance of semiconductors verses critical electric field. Points on the plot represent the ideal parallel plan specific on-resistance for a Schottky diode breakdown voltage of 1000 V.

Figure 2. Specifics on resistance of semiconductors. Adapted from [22].

It should also be mentioned that the thermal conductivity of GaN can also be increased to roughly 200 W/m*k if the GaN is grown on a SiC substrate [16]. Additionally, the thermal coefficient of expansion for GaN is closer to that of the insulating ceramics allowing it to mitigate reliability issues with packaging on ceramic substances [12]. Though

its use in high electron mobility transistors (HEMTs), GaN is also seeing a growing market share in high frequency and high voltage electronics with megahertz capabilities and low-loss switching performance which are attractive to radar and cell phone markets [23].

2. Recombination and Light Emission

A unique property of GaN is light emission, which is produced by a process known as electron-hole pair recombination. More specifically, recombination is the process through which a free electron recombines with a free hole via a direct or multistep process. These processes result in the giving up of energy in the form of a photon or phonon, which may be absorbed by other atoms within the material or will escape the material in the form of heat (in the case of a phonon) or light (in case of a photon) [20]. The recombination of electrons and holes can take place via different methods which determine the form of energy released from the process. Direct band-to-band recombination is the recombination of a free electron in the conduction band with a hole in the valence band of the material with no intermediate step. In direct bandgap materials, this process results in the emission of a photon. Direct excitonic recombination is similar to direct band-to-band recombination in that a free electron in the conduction band combines with a hole in the valence band [24]. However, excitonic recombination is not immediate, but is a secondary result after the capture of a free conduction band electron by a hole. This process also releases a photon, but with less energy than the direct band-to-band recombination due to the bond energy lost in creating the exciton [24]. Excitonic photon missions constitute a majority of the light emission from forward-biased GaN minority carrier devices. The general spectrum of excitonic electroluminescence can be modeled using Equation 5 where *I* is the current magnitude and $E_x(T)$ is the exciton energy [25]. It can also be seen via Equation 5 that the position and magnitude of the peak emission energy of excitonic recombination is a strong function of both current and local device temperature at the point of emission.

$$I_x(\hbar\omega) \alpha I^n \left(\hbar\omega - E_x(T)\right)^\gamma \exp\left(\frac{\hbar\omega - E_x(T)}{kT}\right) \qquad (5)$$

Finally, indirect recombination involves a “third party” (or impurity) within the material that requires less energy to remove valence electrons from its outer shell [24]. Also known as traps, these impurities act as the catalyst or an epicenter to draw the electrons and holes into the same region where they will recombine. Since indirect recombination takes place at a lower intermediary level than the actual bandgap of the material, the energy released from this type of recombination is a phonon.

Direct band-to-band recombination is the primary process used in LEDs, although excitonic recombination (as in the case of GaN) may also contribute to the photonic emissions. Referring to Figure3, LEDs use positively and negatively doped materials to create areas (PN junctions) where the free electrons and holes will collect and recombine. The photon creation of these PN junctions near particular edges of the device also increases the probability that the photons will escape the device in the direction of the nearby edge [3]. Forward- biasing these PN junctions with electrical current adds electrons into the negatively doped regions and holes into the positive regions. Increasing the levels of electrons and holes increases the interactions at the PN junction, resulting in more recombination interactions and the release of more photons.

LEDs are normally optimized to extract the generated light at the expense of other device characteristics, such as breakdown voltage. However, photonic emissions from the PN junction of a power electronic device must travel through the body of the device to exit into the surrounding atmosphere. The optical path length for light emitted within a power device is long compared to LED designs, resulting in large amounts of light reabsorption within the material and reflection of light back into the semiconductor at the device surface.

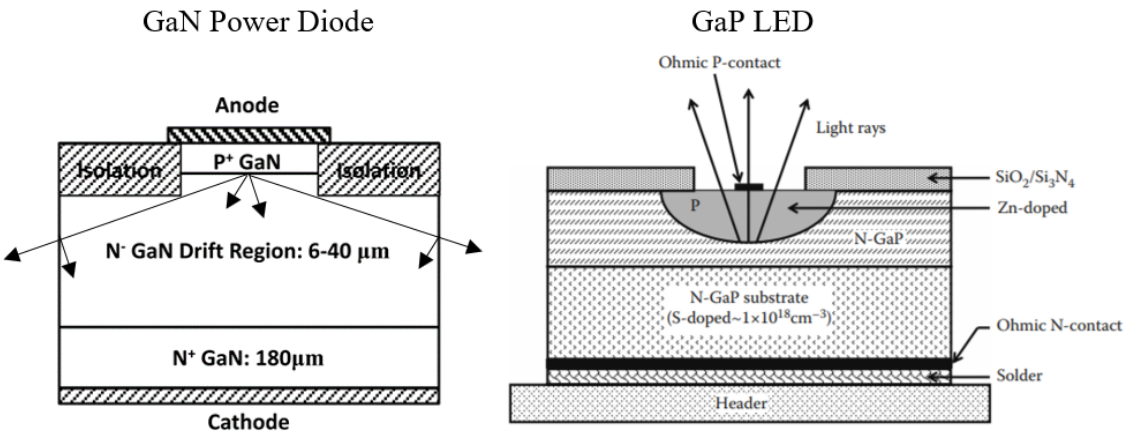

This image depicts the PN junctions of a diode used in power electronic applications where photonic emissions must travel through the drift region to exit the device and a LED with the PN junction placed near the edge of the diode to maximize photon emission in the upward direction.

Figure 3. Cross section of a vertical GaN power diode (left) and red gallium-phosphide (GaP) LED (right). Source: [3], [19].

B. POWER SYSTEMS AND THE BUCK CONVERTER

Evolution of power systems from simple mechanical means to responsive solid-state switching has been substantial in terms of complexity. Systems today must be able to convert and produce constant voltages and waveforms with exceptional accuracy and under varying loads. These loads often require direct current (DC) supplies which are unable to use inductive transformers to vary their output as demands change. In the past, voltage in DC circuits were varied by placing a resistor in series with the circuit. While this produced very accurate control, the power factor would never be able to exceed fifty percent since the resistor would always consume a large portion of the power. This design flaw limited most DC systems in size and scope due to the power loss and heat. Modern power systems accomplish the task of varying DC outputs by emitting pulsed outputs which in a given period will average the desired voltage for that period. These periods may then be reduced to very small segments of time based on the minimal time it takes to switch the power producing device on and off (i.e., to produce a single pulse). And if these periods can be made small enough, each period may be altered to produce a sequence of pulses, identical in magnitude, but will result in an average output equal to the DC output or can be varied

to mimics a waveform. Finally, the use of an integrating device, such as a low pass filter, smooths out the ridged pulses into a flowing transition and yielding an actual continuous wave. The benefits of this system allow for great flexibility, not only to produce any desired waveform, but rapid response times to react to changes in load demand. Additionally, these systems are also of value because they generally are a fraction of the weight and require less space than conventional power systems which employ RLC (resistor, inductor, and capacitor) circuits.

1. The Buck Converter

One common switched power system is the step-down converter, also known as a "buck" converter. This system is of particular interest due to its function of reducing input voltage to the desired voltage of the circuit, which is one of the more common methods used in dc power supplies and motor speed control applications [26]. To control the length of each output pulse, buck converters typically use a comparator in which a repetitive waveform and dc control circuit are fed. The frequency of the waveform determines the period between pulses and length of time each pulse is on during the period. The frequency is controlled by changing the dc control input to the converter. This ratio of pulse duration (t_{on}) to period (T_s) is known as the duty cycle (D) and can be used to derive the expected output voltage (V_o) based on the input (V_d), as shown in Equation 6, which can then be expressed as a function of the duty cycle, as shown in Equation 7.

$$V_o = \frac{1}{T_s}\int_0^{T_s} V_o\,dt = \frac{1}{T_s}\left(\int_0^{t_{on}} V_d\,dt + \int_{t_{on}}^{T_s} 0\,dt\right) = \frac{t_{on}}{T_s}V_d = DV_d \qquad (6)$$

$$D = \frac{V_o}{V_d} \qquad (7)$$

As alluded to earlier, these pulsed outputs are often too harsh to be used by the devices on the load side of this circuit, so an integrating device is placed in the circuit. As depicted in Figure 4, placing an inductor in series, or a capacitor in parallel, or both, creates a low pass

circuit, which would filter out noise within the circuit and ideally changes the pulsed waveform into a continuous wave [26].

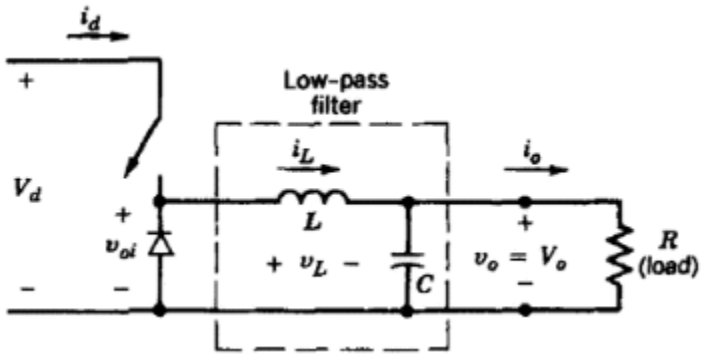

This image depicts a buck converter which uses an inductor (L) and capacitor (C) for low pass filters. While use of a capacitor within a Buck converter is not typical, the schematic illustrates how an inductor and capacitor would appear in the circuit if used.

Figure 4. Buck converter diagram. Source: [26].

In the case of the inductor, the sudden opening of the switch can result in large voltages as the inductor attempts to maintain the current of the circuit. These spikes can create excessive heating and arcing, resulting in damage to the converter as well as the load. To avoid these voltage spikes, a diode, known as a flyback diode, is placed in the circuit. The flyback diode will forward bias once the switch opens and thereby limit the voltage of the inductor. Hence, the diode is required for the use of the inductor. Use of wideband semiconductors are ideal in this type of circuit to handle faster speeds, higher voltages, and heat generation. Control of the switching duty cycle is based on monitoring or voltage or current of the circuit. However, this switching process is notorious for the EMI it generates, and it follows that the most common sensors used for monitoring these power circuits are vulnerable to EMI.

Designers choosing between voltage control and current control must consider the advantages and disadvantages of each option. Voltage control sources require a single feedback loop and are generally easier to design. Voltage control sources also possess a low-impedance power output that results in more consistent cross-regulation of multiple loads [27]. However, the need of these control sources to first sense errors via the feedback

loop before responding yields slower response times. Voltage control must also consider the addition of poles due to an output filter which can be dominant at low frequency roll off or another zero that must be considered. On the other hand, current control offers faster dynamic response and the addition of only one pole which much be accounted for in the design. The trade is in complexity as two feedback loops are required, greater susceptibility of noise within the control loops, and poorer cross-regulation of multiple outputs.

2. Hall Effect Current Sensors

Another known vulnerability of many control systems is the use of Hall-Effect current sensors. Of the two methods for obtaining current data, designers generally favor external sensors since in-line sensors are typically not designed to handle higher currents, their impedance can affect the circuit, and there are extra labor and safety requirements when replacing these components. In contrast, external sensors, such as the Hall-Effect sensor as depicted in Figure 5, are low cost with a relatively simple design that provides fast response times and robustness [28]. These sensors are mounted externally and can be used in high power applications. Additionally, these sensors can fail and be replaced without affecting the circuit. However, there are drawbacks to the application of this device as the Hall-Effect current sensor is extremely susceptible to EMI, particularly when the interference is propagating parallel to the surface of the sensor [29]. It is with this obstacle of EMI in mind that this thesis investigates the use of GaN light emission.

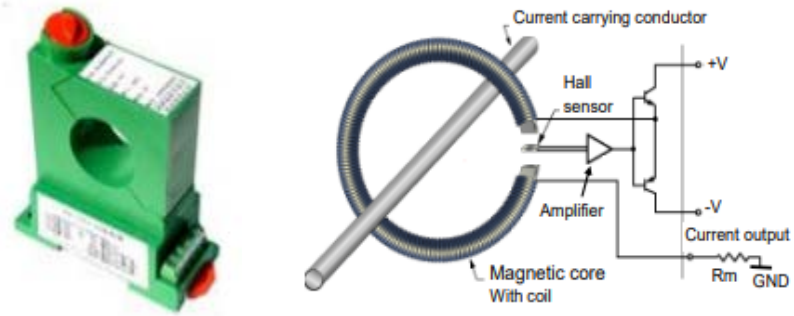

Figure 5. Hall effect current sensor and schematic. Source: [28].

III. EXPERIMENTAL DESIGN AND CALIBRATION

A. THE GALLIUM NITRIDE DUT

The device under test (DUT) is a vertical GaN diode grown using metal organic chemical vapor deposition (MOCVD) [13], [25]. This DUT was procured from the same batch of devices studied by Maeve Broeg and whose spectral analysis is referenced in the next section for the selection of optical filters [13]. The 40 μm drift region contains an n-type doping of 2–5 x 10^{15} cm^{-3} on top of a 180 μm thinned bulk n+ doped GaN substrate. Over the drift region is a 0.5 μm p+ layer doped to 2 x 10^{19} cm^{-3} with Mg. Ion implantation was used to form the edge terminations followed by e-beam deposition to lay the 0.0048 cm^2 ohmic contact; this is packaged in a TO-257 die on a 1.2 mm copper interposer. Properties of the diode are given in Table 2.

Table 2. GaN vertical diode characteristics. Source: [25].

Forward Voltage V_{on}	3.1 V
On Resistance R_{on}	0.2 Ω
Breakdown Voltage V_{br}	1200 V

B. INITIAL SYSTEM AND EXPERIMENTAL DESIGN

Design of a testing system employed in this research began with the premise of a buck converter (similar to Figure 4) with use of a vertical GaN diode as the flyback diode. As such, the diode would be forward biased during the “open switch” cycle of the circuit and would be driven by the power of the inductor, which would be functioning as a current source. The initial testing setup is depicted in Figure 6. Power to be fed through the diode was controlled with a voltage controlled current source (VCCS) to allow use of the Agilent 33220A function generator and remote control via a GPIB connection to produce desired changes in current through the diode. Design of the current source to be used was built in accordance with a design by Krupa and Gasior that placed a calibrated 25W 1Ω resistor in series with the diode [30]. Light from the diode was captured by a multifiber optical cable, which then passed the photonic emissions through optical narrowband filters and to two Si

photodiodes. Output from the photodiodes was increased using low noise amplifiers (LNA) and then routed to the Keysight DSOX3014T oscilloscope.

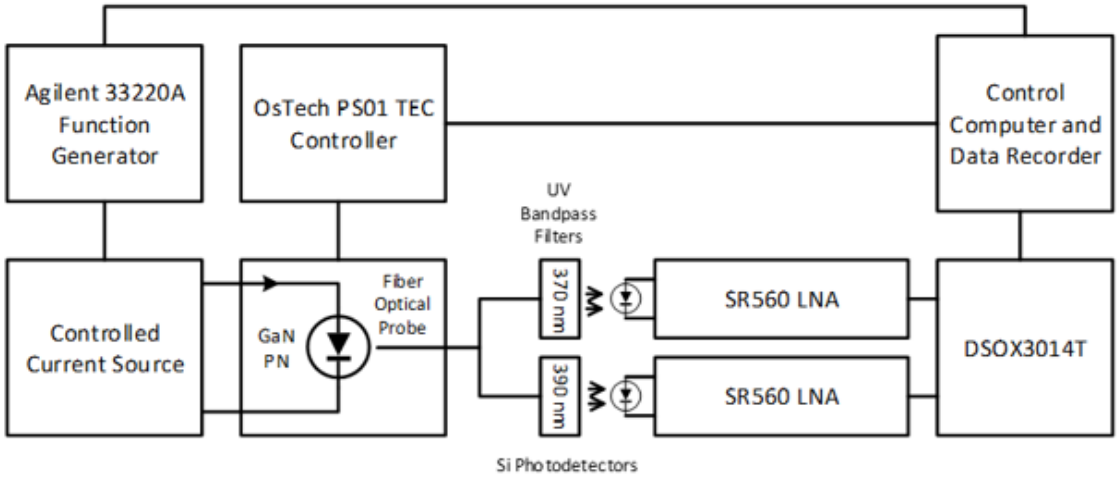

Figure 6. Initial testing system setup.

Testing was conducted using National Instruments (NI) Laboratory Virtual Instrument Engineering Workbench (LabVIEW) software with drivers able to control the function generator and the thermoelectric cooler (TEC) control unit for measuring and adjusting the temperature of the GaN diode baseplate using USB/GPIB connections. LabVIEW also collected and recorded data from the oscilloscope. Optical filter selection was based on research by Maeve Broeg, shown in figures 7 and 8, which identified four possible emission peaks.

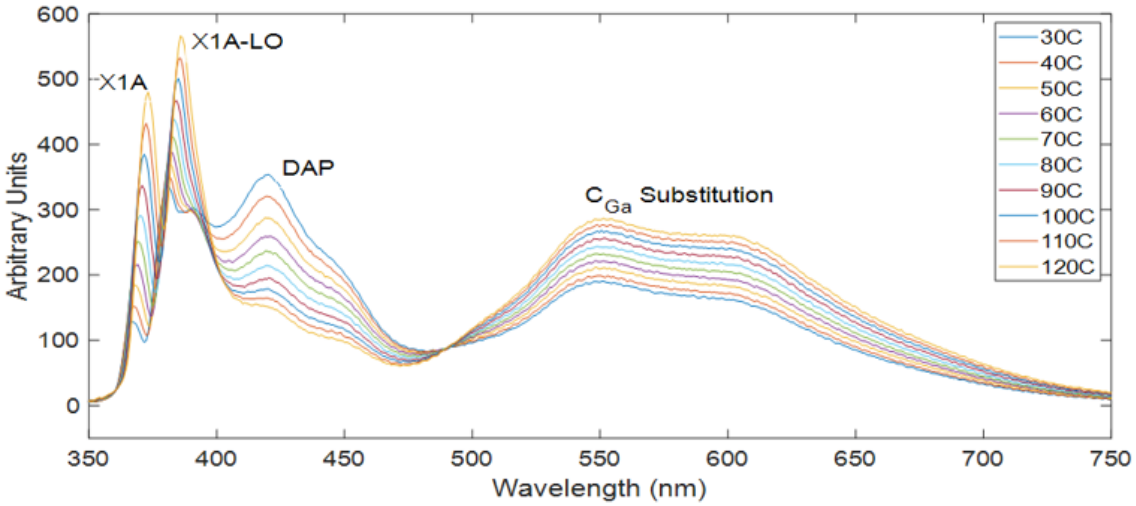

Figure 7. Spectrum emissions of a GaN PN junction with variation in temperature. Source: [13].

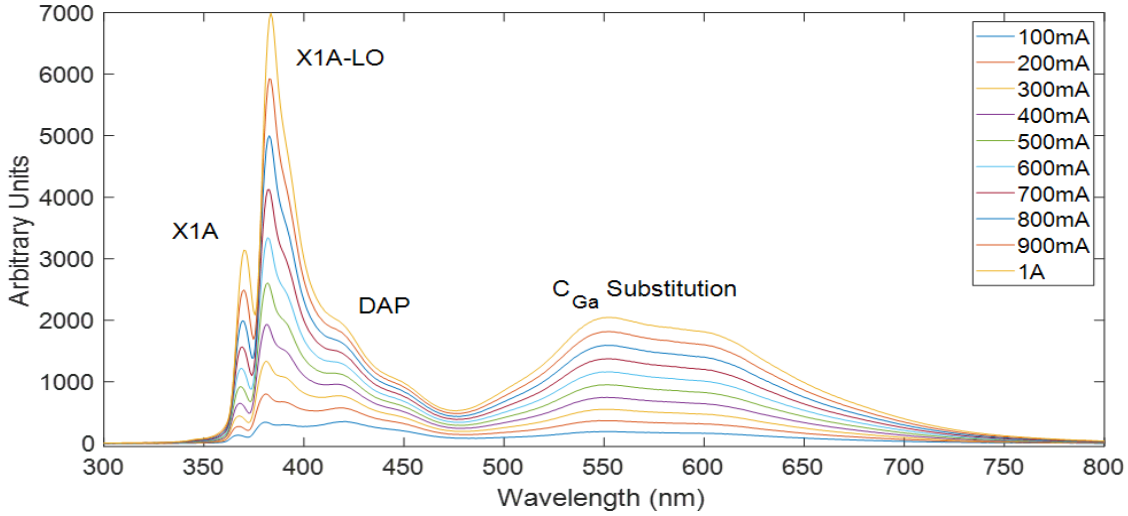

Figure 8. Spectrum emissions of a GaN PN junction with variation in current. Source: [13].

In the measured current and temperature spectrums above, X1A with the shortest wavelengths would be the yielded emissions from direct bandgap recombination [13]. Next is the X1A-LO peak with a slightly larger wavelength with some of the energy being expelled as heat during excitonic recombination. The final two peaks resulted from impurities within the material. The donor-acceptor-pair (DAP) peak was assessed by Broeg to correspond with magnesium (Mg) impurities within the device, and from carbon (C_{Ga})

which was used during the MOCVD fabrication [13]. For testing, the X1A and X1A-LO peaks were selected as these emissions corresponded directly with emissions from the GaN. Use of the DAP and C_{Ga} substitution peaks are possible; however, these emissions are likely to have greater variance between subsequent devices, since these emissions are related to impurities within the device.

Results from this initial setup testing allowed for calculations of current and temperature. However, applicability was an issue because of the microampere photodiode outputs which required amplification to the point that the gain bandwidth product limited frequencies to less than a few hundred Hertz. With switching of power systems exceeding 20kHz, this initial design would be insufficient to meet even minimal needs of most power systems. Since the limiting factor primarily resided with the gain bandwidth product of the amplifiers, the use of lock-in amplifiers was explored.

C. CURRENT SYSTEM WITH THE USE OF LOCK-IN AMPLIFIERS

1. Explanation of the Lock-In Amplifier

Lock-in amplifiers use phase sensitive detection (PSD) to detect very weak signals. This process is applicable with signals of just a few nanovolts obscured by significant signal-to-noise ratios [31]. Use of PSD required a reference signal in addition to the input signal. The PSD technique then multiples the two signals together. Representing a sinusoidal as $V\sin(\omega t + \theta)$ where V is the amplitude of the signal, ω is the frequency of the signal, t is time, and θ is the signal phase; the product of the two signals can be written as shown in Equation 8 and then rewritten in terms of the cosine (Equation 9).

$$V_{PSD} = V_{ref}\sin\left(\omega_{ref}t + \phi_{ref}\right)\cdot V_{sig}\sin\left(\omega_{sig}t + \phi_{sig}\right) \quad (8)$$

$$V_{PSD} = \frac{1}{2}V_{ref}V_{sig}\cos\left(\left[\omega_{sig} - \omega_{ref}\right]t + \phi_{sig} - \phi_{ref}\right) - \frac{1}{2}V_{ref}V_{sig}\cos\left(\left[\omega_{sig} + \omega_{ref}\right]t + \phi_{sig} + \phi_{ref}\right) \quad (9)$$

Since the frequency of the signal (ωsig) and the frequency of the reference (ωref) will be the same, the cosine of the frequency differences is reduced to one; and with the use of a low pass filter, the latter half of the equation containing the frequency sum can be

removed. The result is stated in Equation 10, which varies solely on the phase difference and amplitude of the two signals and yielding a DC output, provided these two variables are held steady.

$$V_{PSD} = \frac{1}{2} V_{ref} V_{sig} \cos\left(\phi_{sig} - \phi_{ref}\right) \tag{10}$$

The flaw in this single function is the PSD output decreases to zero as the phase difference of the signals approaches 90 degrees (π/2 rad). To address the possibility of a reduction in output due to a phase difference, a second reference signal with a 90-degree phase shift from the first reference signal is multiplied with the input signal as shown in Equation 11.

$$V_{PSD2} = \frac{1}{2} V_{ref} V_{sig} \cos\left(\phi_{sig} - \phi_{ref} + 90\right) = \frac{1}{2} V_{ref} V_{sig} \sin\left(\phi_{sig} - \phi_{ref}\right) \tag{11}$$

Hence, the two proportional outputs in forms of sine and cosine of phase offset can be used to calculate a magnitude and phase offset from equations 12 and 13.

$$V_{mag} = \sqrt{V_{PSD}^2 + V_{PSD2}^2} \tag{12}$$

$$\phi = \tan^{-1}\left(\frac{V_{PSD2}}{V_{PSD}}\right) \tag{13}$$

This manipulation of the input signal into its first harmonic by the lock-in amplifier can be demonstrated mathematically using the Fourier transform. Ideally, the switched converter will result in a square wave input. Taking the Fourier transform of a square wave using the variables defined in Figure 9 results in the harmonic function listed in Equation 14, where $2T_1/T_0$ is defined as the duty cycle (D).

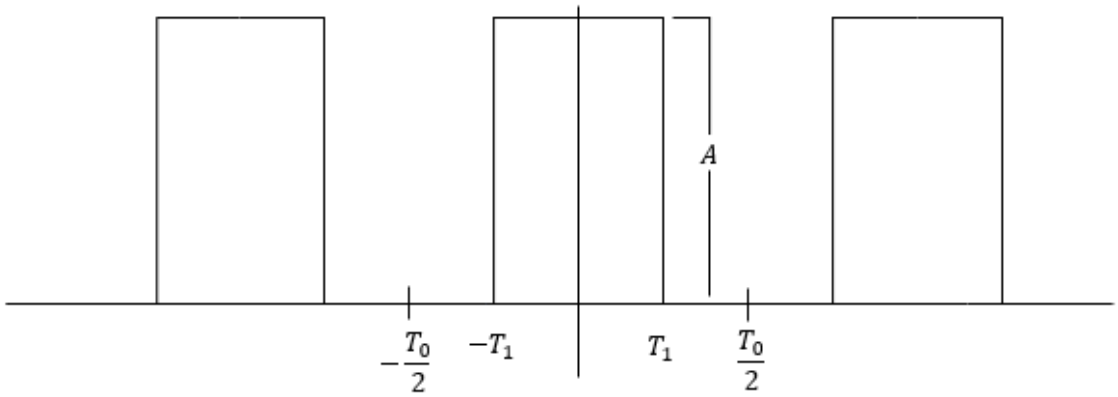

Figure 9. Ideal square wave input.

$$C_n = \frac{1}{T_0}\int_{-\frac{T_0}{2}}^{\frac{T_0}{2}} Ae^{-j2\pi nf_0 t}dt = \frac{A2T_1}{T_0}SINC\left(n\frac{2T_1}{T_0}\right) = ADSINC\left(nD\right) \qquad (14)$$

Since the lock-in output is the first harmonic of the signal, *n* would be zero and the sinc function is equal to one. This then leaves the DC output (AD), which is a function of the amplitude and duty cycle and the average output for the period (T0). Experimentally, the input will be the discharging of an inductor, which will resemble a square wave but will exhibit an exponentially declining (1-ex) amplitude. However, this decline may be assumed to be linear provided a large enough inductor is used and the discharge duration of the inductor (T1) allows for a small discharge of the total inductor field. Figure 10 displays the expected signal produced from the current through the flyback diode and is followed by Equation 15, with the result of the Fourier transform of this signal that now has a real and imaginary component.

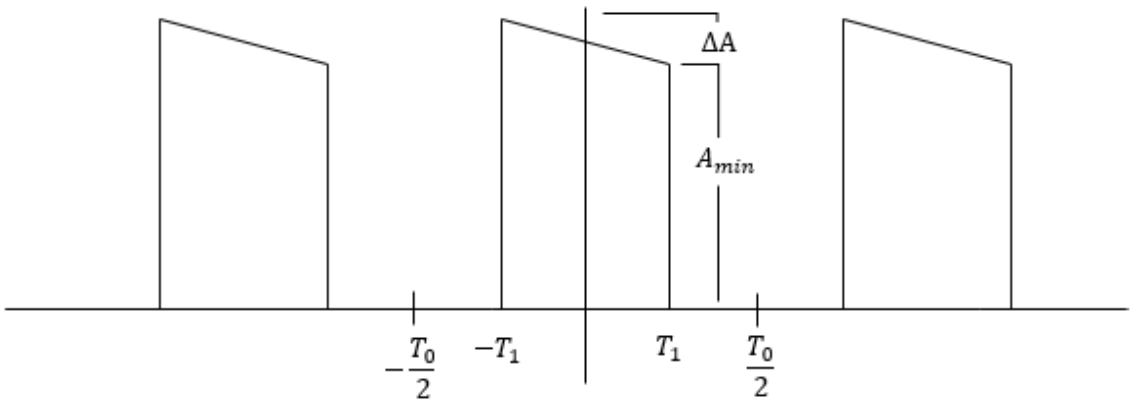

Figure 10. Expected flyback diode waveform.

$$C_n = \frac{-\Delta A}{2T_0T_1}\int_{-\frac{T_0}{2}}^{\frac{T_0}{2}} \tau e^{-j2\pi nf_0\tau}d\tau + \frac{\Delta A + 2A_{\min}}{2T_0}\int_{-\frac{T_0}{2}}^{\frac{T_0}{2}} e^{-j2\pi nf_0\tau}d\tau$$

$$= \left(\frac{\Delta A}{2} + A_{\min}\right)\frac{2T_1}{T_0}SINC\left(n\frac{2T_1}{T_0}\right) - j\frac{\Delta A\cos\left(2\pi nf_0T_1\right) - \Delta ASINC\left(n\frac{2T_1}{T_0}\right)}{2\Pi n} \qquad (15)$$

$$= \left(\frac{\Delta A}{2} + A_{\min}\right)DSINC\left(nD\right) - j\frac{\Delta A\cos\left(2\pi nf_0T_1\right) - \Delta ASINC\left(nD\right)}{2\pi n}$$

Viewing Equation 15 from the standpoint of the first harmonic (n=0), the imaginary component is zero and the real component again becomes the function of the amplitude and the duty cycle where the output is the average amplitude of the period (T_0). Referring back to the use of the lock-in amplifier, this averaged output is another good fit with the switched power converter, as it is the average output from the switching that is desired.

2. Testing System Design

Incorporation of the lock-in amplifier into the monitoring of a potential power converter system seems a logical fit, as the switched source modulation matches what is needed by the lock-in amplifier along with a known reference input to be obtained from the switch controller. The weak signal detection of the lock-in amplifier technique avoids the gain bandwidth product limitations and was easily incorporated into the testing system

by replacing the low-noise amplifiers with the lock-in amplifiers as shown in figures 11 and 12.

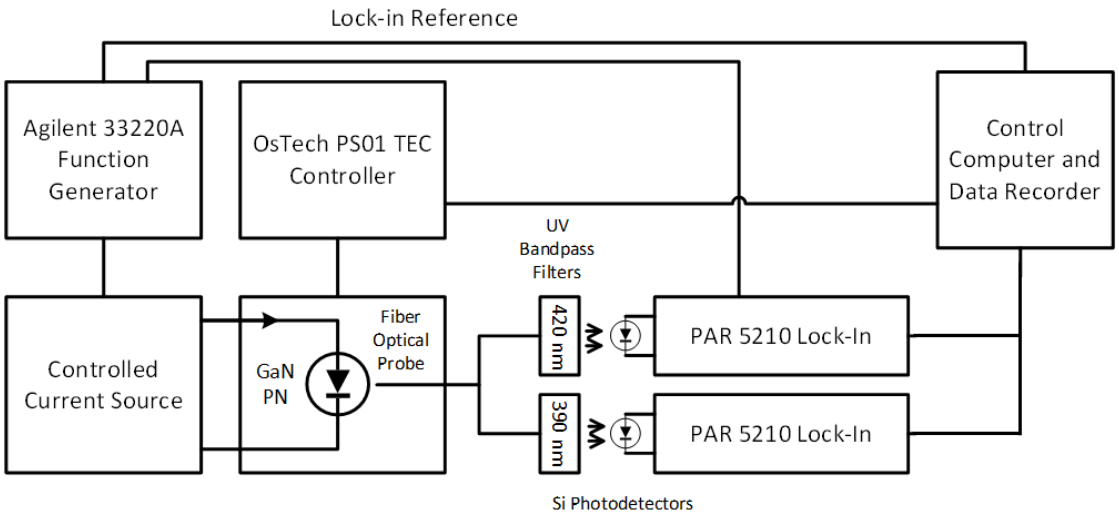

Figure 11. Schematic of the lock-in amplifier testing system. Source: [25].

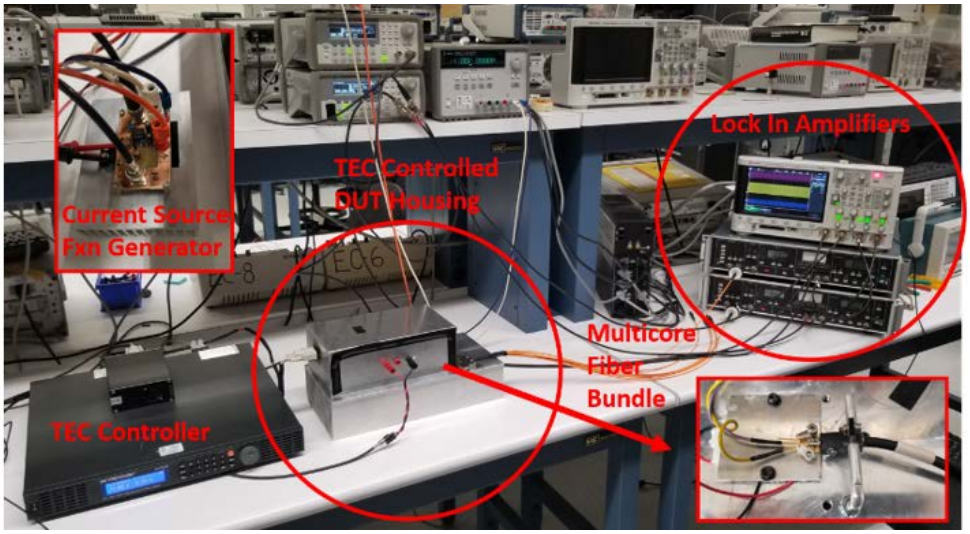

Figure 12. Image of the lock-in amplifier testing system. Source: [25].

In this modified setup, the Agilent 33220A, again, produced the desired pulses or waveforms that feeds into the LM741 op-amp controlled gate drive of the VCCS for a current output to the diode. Shown in Figure 13, the DUT was mounted on 50 mm x

50 mm aluminum plate which sits on top two CUI CP85338 TEC coolers controlled by the OsTech PS01 TEC controller. The temperature probe of the TEC was attached on the inside of the TO-257 die cavity. A 1-to-7 400 µm solarized multifiber optical cable was then affixed with its exposed fibers near the side of the device to capture light emissions from the DUT.

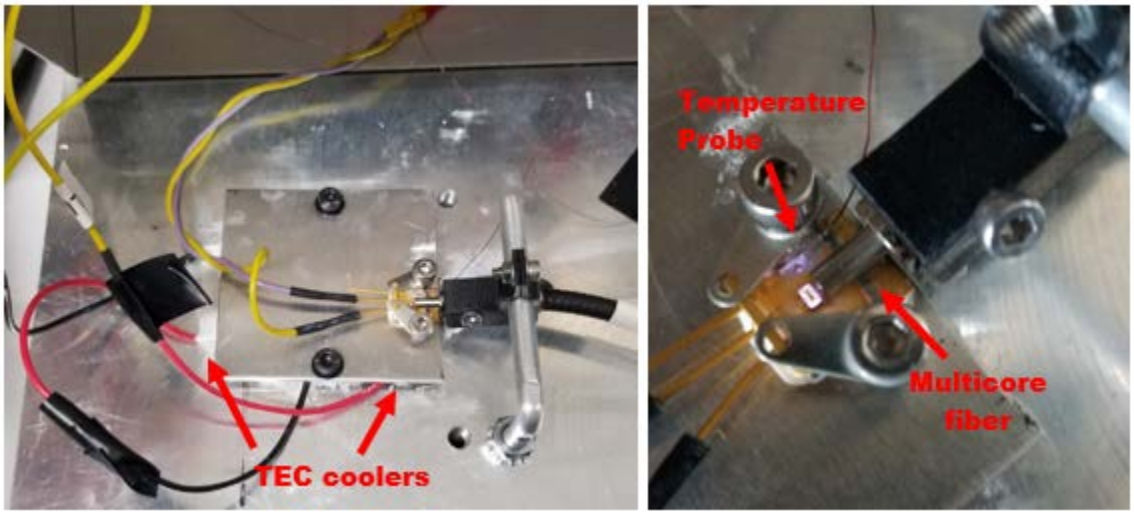

Figure 13. Dark box setup and light emission capture.

On the other side of the fiber, the emissions were passed through a narrow band optical filter then on to the photodiode. With the exception of the 550 nm filter with a 40 nm bandwidth, the filters possessed a 10 nm bandwidth and have had caps of the filter casing 3D printed to minimize the space between the fiber and the filter, and between the filter and photodiode. Figure 14 depicts the changes in the filter casing. These modifications resulted in an approximate gain of three times the values produced while using the manufacturer case.

Figure 14. 3D printed optical filter case caps used to narrow fiber to filter gaps.

The UV sensitive Thorlabs FDS010 photodiode on the back side of the filter covered a 320–1100 nm range with a nanosecond response time and was connected directly to the lock-in amplifier. Two Princeton Applied Research SR5210 lock-in amplifiers were then used to analyze the output of two different optical filters with the data collected via a LabVIEW program. Of note, the Keysight DSOX3014 oscilloscope seen in Figure 12 was used only for visual observations during the calibration and testing.

3. Calibration

Several LabVIEW programs were used in the control of the function generator and TEC temperatures as well as in the calibration data logging over a current range of 0.2 A to 4 A and a temperature range of 20 °C to 110 °C [25]. Short burst of 1 kHz square wave current inputs using a 50% duty cycle were fed to the DUT during each step of the testing. Pauses in the input signal allowed for changes in temperature and/or current settings between steps and to avoid device heating. The lock-in outputs were then collected for each filter using 50 mA current increments and 5°C temperature increases. Next, MATLAB was used to determine a best fit polynomial for the matrix of temperature and current values. Figure 15 shows the fitted surfaces for the 390 nm and 420 nm data. Images of surfaces for all tested optical filters can be found in Appendix A.

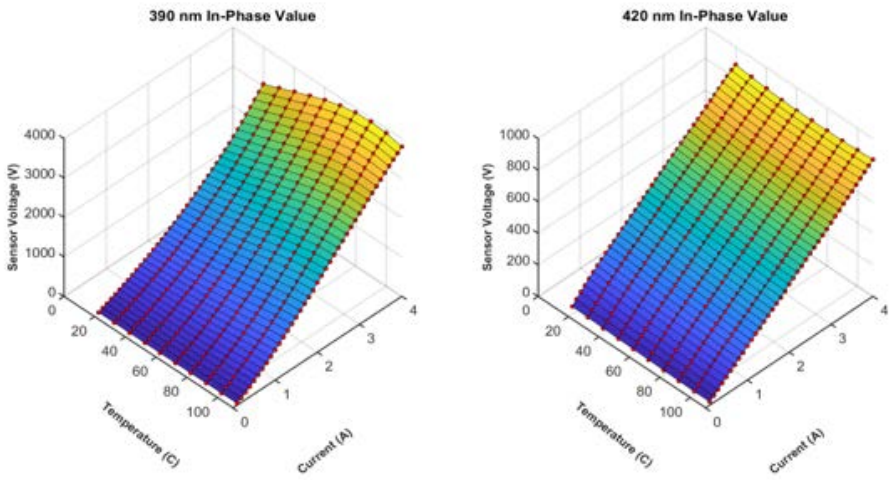

In the two surfaces above, the colored surface represents the measured surface while the red dots are the fitted polynomial solutions at each test point. In the example above, a 7th order polynomial was applied to the 390 nm surface, while a 5th order polynomial was applied to the 420 nm surface [25].

Figure 15. Calibration and best-fit polynomial surfaces for the 390 nm and 420 nm optical filters.

In the surfaces depicted above, the 390 nm surface used a 7th order polynomial, and the 420 nm surface was fitted with a 5th order polynomial [25]. Use of these surfaces or their associated polynomials cannot be extended past the calibration ranges due to the oscillatory nature of the polynomial. These surfaces were then used to calculate the current and die temperature of various waveforms; however, it should be mentioned that this leads to the proper selection of filters to help in the reverse calculations. The goal is to find two filters with a large variation in their surfaces and with unique crossings within the expected range to ensure better precision. Figure 16 provides a good example of the desired variation in the slopes. This example also depicts the narrowing of this variation toward the lower currents as the traces approach similar slopes. It is also conceivable that a non-unique solution may be possible. In such an instance narrowing of the scope of the solution or the use of another filter would help to determine the correct current and temperature. Additional filters could also be utilized, but the designer would have to weigh the cost of time and processing power needed for processing the extra calculations. Plots of calibration curves for all of the tested filters can be found in Appendix B.

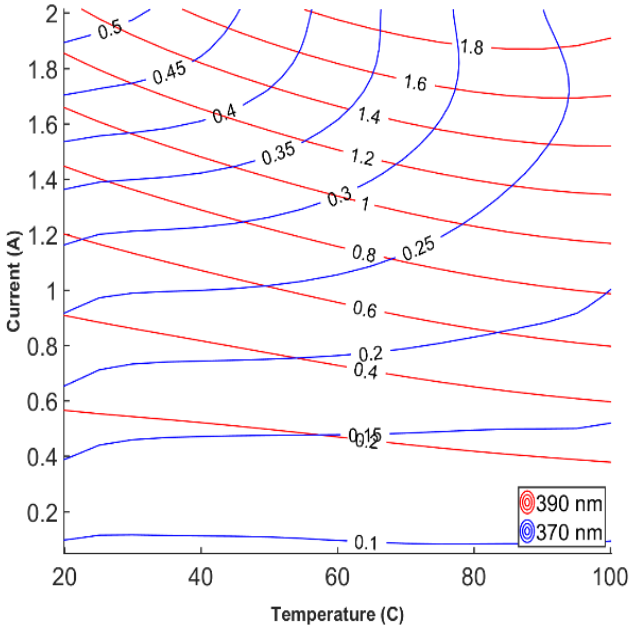

Figure 16. Plot of the 370 and 390 nm current versus temperature curves.

4. Avalanche Photodiodes

One later modification of the testing system was the shift from the initially used UV sensitive Thorlabs FDS010 photodiode to the APD130A2 temperature-compensated avalanche photodiode. This change increased the photodiode output by just under four times using a four-amp input at the DUT. Despite this increase in output voltage, the avalanche diode does exhibit a decrease in sensitivity as seen in the 370 nm surface plots of Appendix A where use of the avalanche diode yielded multiple extraneous values which rendered this surface unfeasible for calibration. In the use of optical filters with higher outputs, the change from a current to voltage input yielded no visually apparent improvements in the calibration surfaces. This change is necessary for future development in which the lock-in amplifier will be replaced by a microcontroller using analog to digital (A2D) inputs. Calibration surfaces and current to temperature plots with the use of the avalanche diodes are contained in Appendixes A and B.

IV. RESULTS

A. REVERSE CALCULATIONS OF WAVEFORM OUTPUTS

With use of the calibration data, output from various waveforms could be analyzed. Analysis was conducted using MATLAB. Highlighting the primary commands used in the analysis program, the “polyfitn” function was first used to determine best-fit polynomials for the surface of the data for each optical filter. The coefficients of the two surface polynomials were then placed into a matrix using the “matlabFunction” command. With the polynomial coefficients, prediction of current and probe temperature from testing could be made with the use of the “fsolve” nonlinear solver function. The “fsolve” function uses a solver based upon Newton’s method, which requires an initial “guess” from which to start its iterations. Hence, the closer the reference, the better the predictions of the solver, to which the previous calculated step was entered as the reference point of each sequential calculation. For the initial calculation, the reference used a temperature of 20° C and a current of 100 mA.

B. STEP RESPONSE

Step response testing consisted of a 2 A current applied to the DUT with no temperature control by the TEC coolers applied and monitored for a period of 150 seconds (s) [25]. Sequential step tests explored various time constant/integration settings of the lock-in amplifier from 3 ms to 30 ms, as shown in Figure 17. The steady state current prediction of all three test were within 0.6% of the measure value.

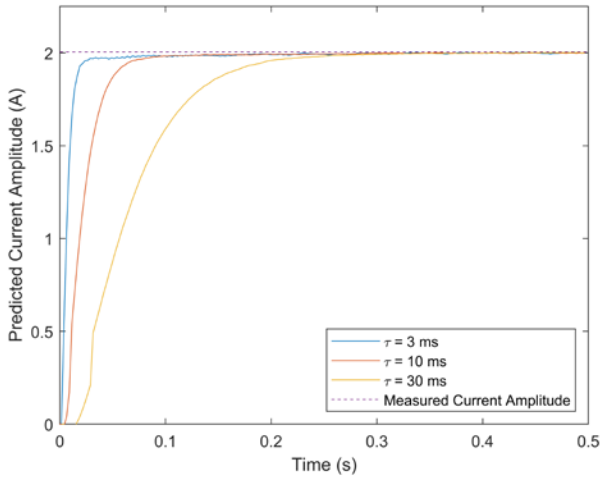

Figure 17. Predicted current during a 2 A step response. Source: [25].

Next step responses were conducted by varying the current input from 1.0 A to 3.5 A in 0.5 A increments for periods of 150 s, again with no external temperature regulation [25]. Results can be viewed in Figure 18. Current error suggests a possible increase with increases in current, although this may be a point within the calibration curve with greater deviation due to the polynomial used. In either case, the average error remains just under 0.54%, even with the exclusion of the outlier at 1.5 A. Temperature predictions were less accurate, with more deviation, and resulted in a 2.5% calculated error (roughly 0.9 °C) offset that was noted here and in other tests.

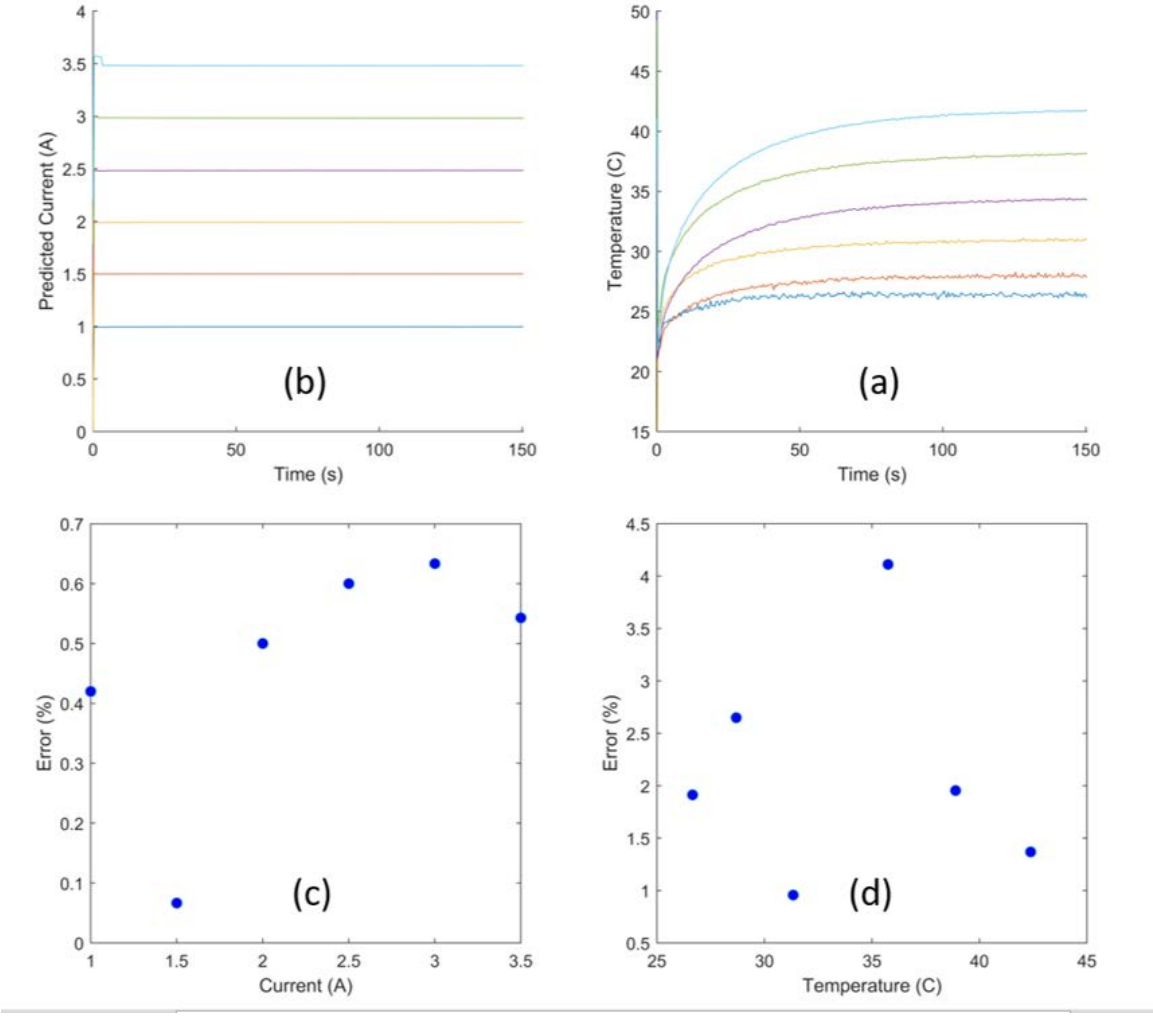

Figure 18. Step response of 1.0 A- 3.5 A inputs. Source: [25].

C. STABILITY

Stability testing applied a 2.5 A current for approximately one hour with no temperature control of the base plate. As shown in Figure 19, predicted steady state current was 2.48 A, with no noted variations in the predicted value over the course of the testing [25]. Temperature predictions, likewise, followed consistently with readings from the temperature probe. However, the predicted temperature offset was again noted between the measured and predicted values.

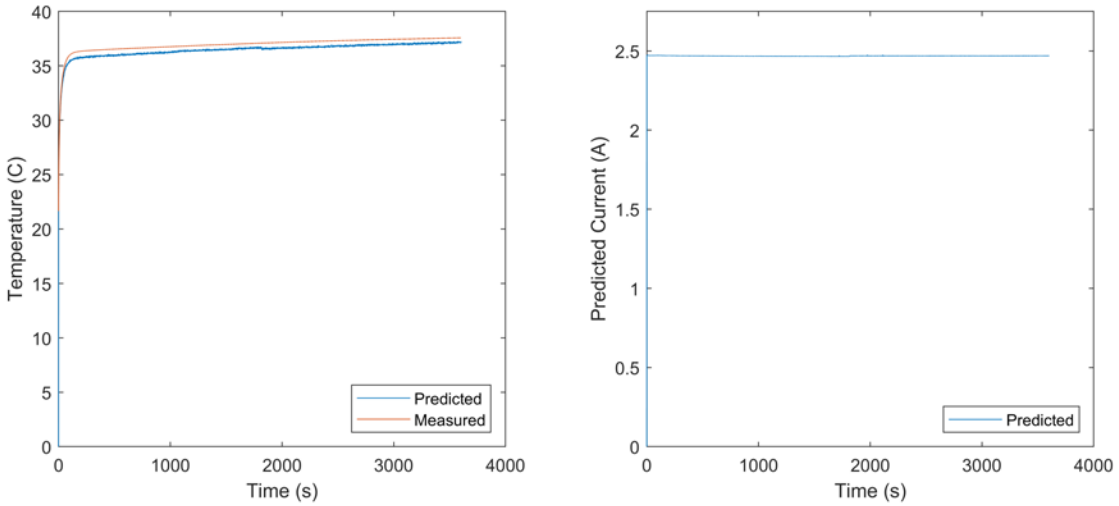

Figure 19. One-hour stability current and temperature results. Source: [25].

D. TIME DEPENDENT MODULATION

Time-dependent testing employed current modulation with a triangle waveform and then temperature modulation via a sinusoidal waveform. The triangle waveform was given a 0.5 Hz, 1 A peak-to-peak amplitude centered at 2 A [25]. Figure 20 displays current rising and falling with temperature variation. Errors in temperature during the abrupt changes were due to some lag in the probe readings because of the time required for heat transfer. Since a slow rate-of-change was applied to temperature changes, this difference should have been minimal. This assumption holds true during the rising and falling periods of the waveform. Therefore, the observed increase in error during the transition from rising to falling temperatures is assessed to be due to integration in the circuitry of the lock-in amplifier. Effects of integration will be discussed in greater detail later in Chapter IV under the section on hysteresis.

Temperature modulation occurred by varying the setpoint of the TEC controller and are shown in Figure 21. With the current through the DUT set at 2A, commanded setpoints of the TEC coolers were varied with a 0.1 Hz, 10 °C peak-to-peak sinusoidal waveform centered at 40 °C [25]. Use of a low frequency was again employed to compensate the slower update times of the temperature probe and to allow adequate times for heat transfer from the DUT to the die base plate where the probe was mounted. Rising

and falling agreement between measured and predicted values tracked well, although the offset error was still present. Variation in the predicted current was not viewed in separate observations on the oscilloscope and assessed in the APEC conference submission as due to discrepancies between the best-fit polynomial surface used and actual calibration surface [25]. Recent simulations have confirmed this assumption with the use ideal calibration inputs and simulation lock-in amplifiers resulting in similar current oscillations as temperature was modulated (Figure 22). Noting that total error between the actual and predicted current never exceeds 1%, the variations are of little concern and only visible due to the y-axis magnification of the graph.

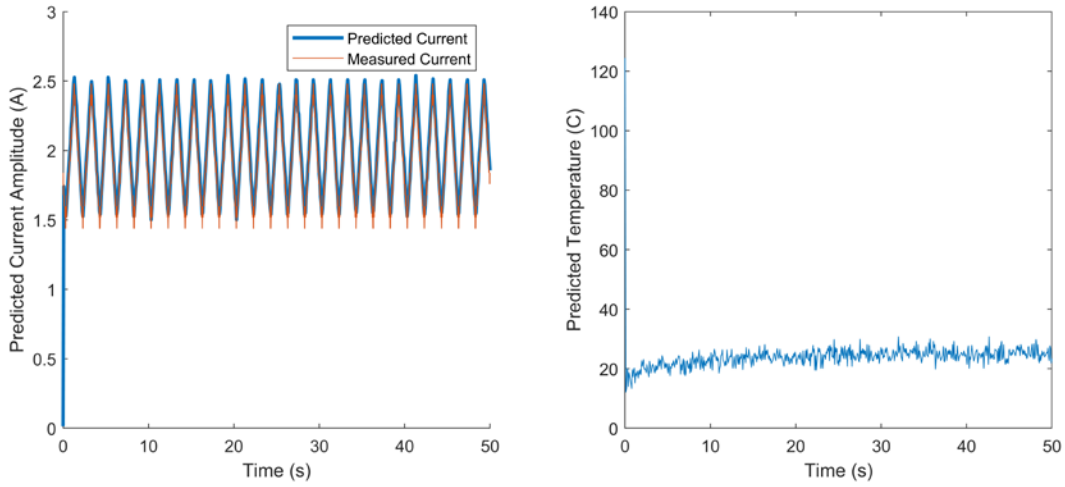

Figure 20. DUT current modulation using a triangle waveform. Source: [25].

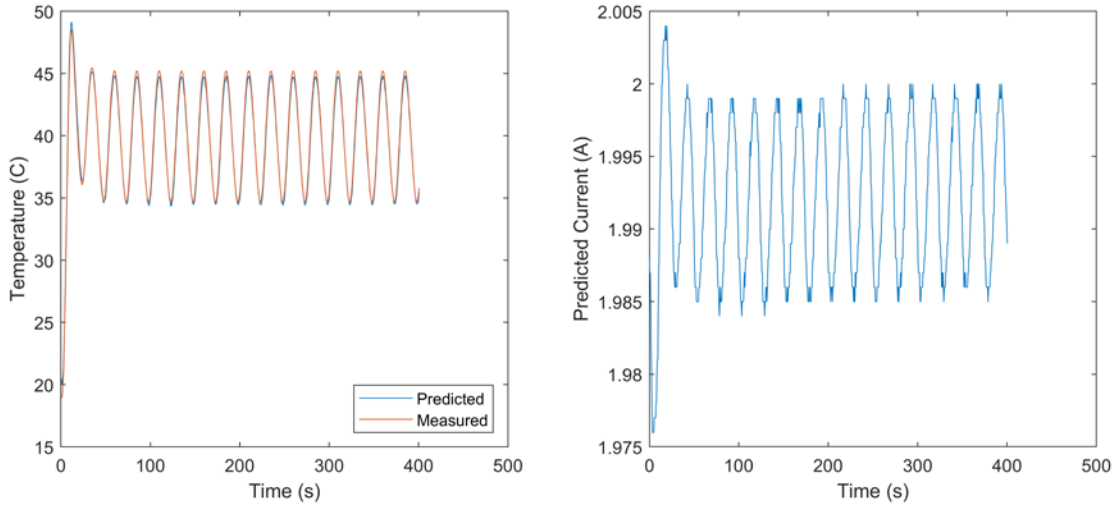

Figure 21. DUT temperature modulation using a sinusoidal waveform. Source: [25].

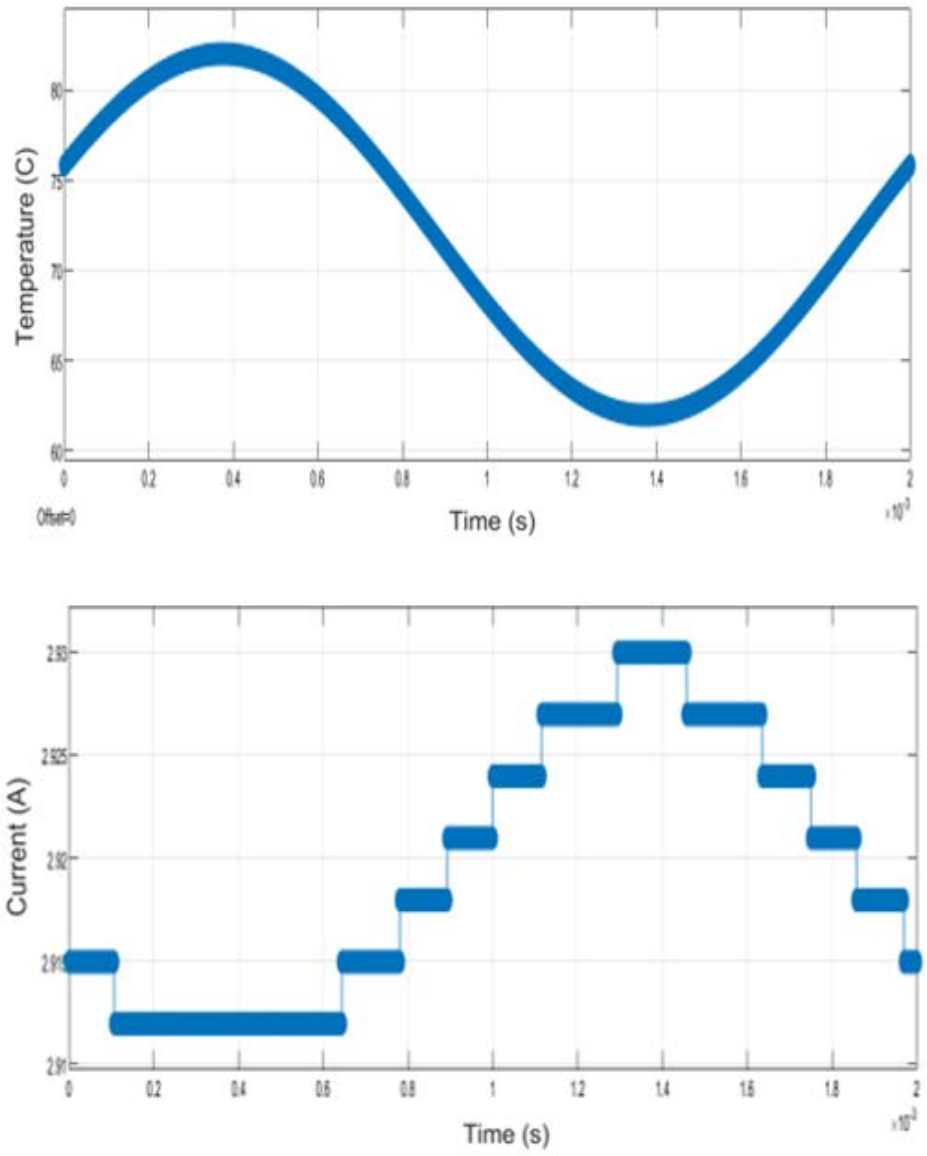

Simulations using an ideal input to simulated locked-in amplifiers resulted in the same slight variation in current while only temperature was modulated. This simulation helps to confirm the current oscillations are due to imperfections in the calibration surface used for predictions.

Figure 22. Simulated temperature modulated using a sinusoidal waveform.

E. DUTY CYCLE MODULATION

Duty cycle (pulse-width) modulation incorporated the use of two function generators with one generator driving the pulse-width output of the second generator. Output of the second function generator, operating at a fixed frequency, would then drive

the VCCS and current to the DUT. In Figure 23 the output duty cycle of the second generator was modulated between 20% and 80% by a 0.2 Hz signal from the first [25]. In-phase outputs from the lock-in amplifiers were then recorded using the 370 nm and 420 nm filters. For plotting purposes, the outputs were scaled up by a factor of 1000 and the fit curve normalized to the 50 % duty cycle.

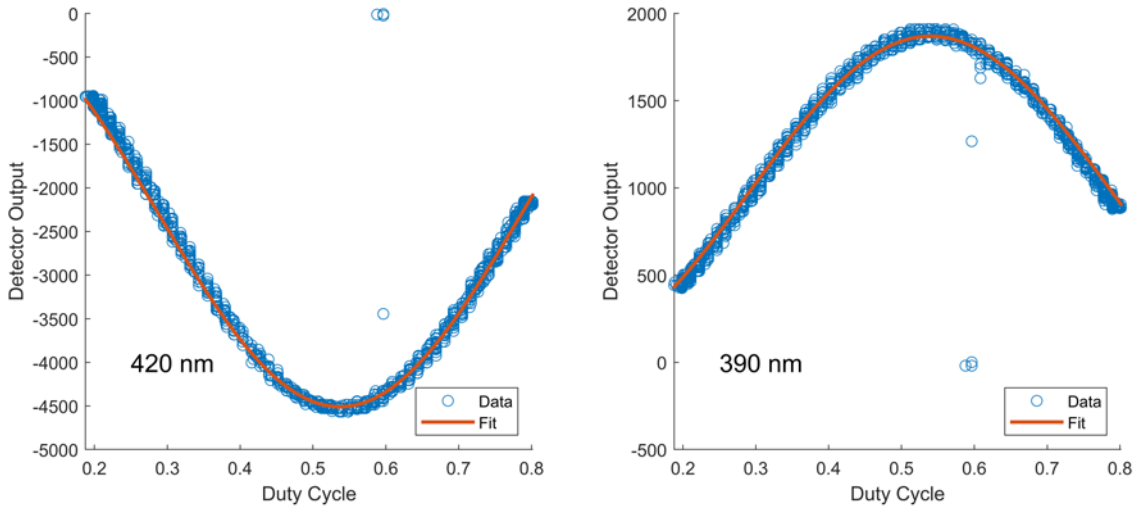

Figure 23. Duty cycle modulation results. Source: [25].

Accuracy predictions of small duty cycle changes were then monitored by having 2 A, 1 kHz pulses input to the DUT using a 0.2 Hz, 10% peak-to-peak duty cycle modulation centered on 50% [25]. Temperature of the base plate was held at 20 °C by the TECs. Recorded in-phase lock-in outputs plotted against pulse-width modulation can be seen in Figure 24. Figure 25 contains predicted current and temperature values plotted against the duty cycle modulation. As noted in previous results, “leakage” and increased errors around the abrupt changes in current are observed; however, all errors in predicted values remained less than 1% of the actual current. Probe temperature was not recorded during this test, but predicted values rose and approached a steady state as expected.

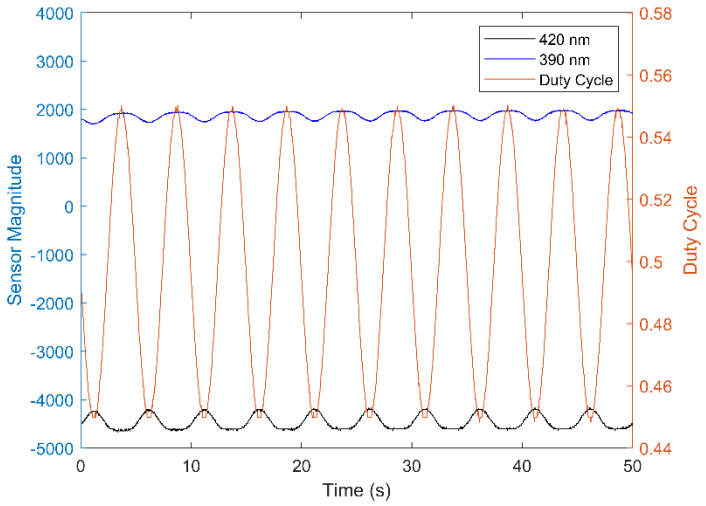

Figure 24. Sensor outputs during duty cycle modulation. Source: [25].

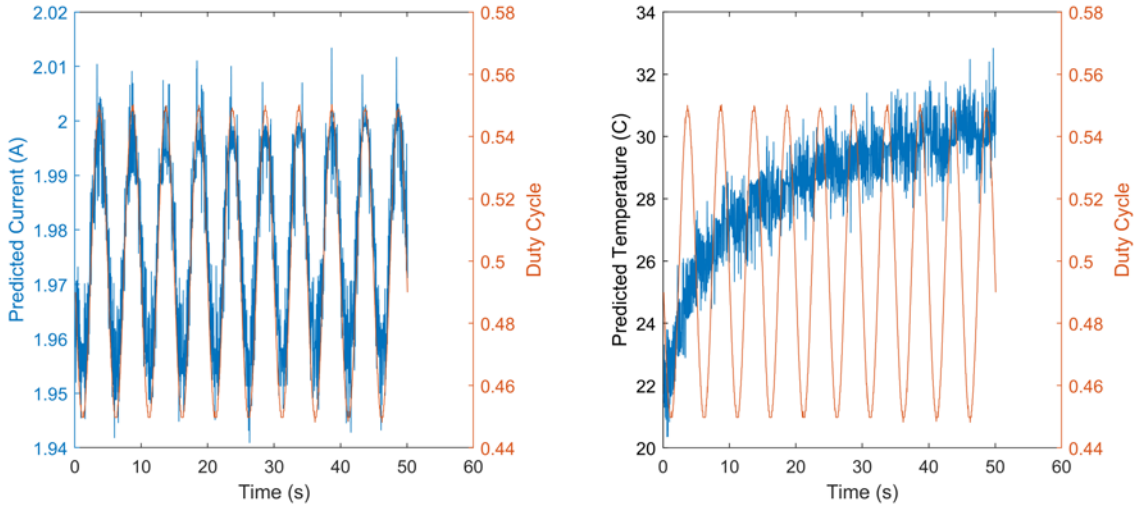

Figure 25. Current and temperature predictions during duty cycle modulation. Source: [25].

F. HYSTERESIS

From Chapter II, switched power converters employ fixed amplitude pulse-width modulation for production of desired waveforms via an averaged output that is integrated or smoothed out via a low-pass filter. Consequently, the ability to track duty cycle modulation within a power system control loop is crucial. Time constant/integration is used to filter out noise from the input signal, but it also limits the lock-in amplifier output

response. The lock-in amplifier response, however, may be slower than the power converter switching frequency since power electronic applications operate under average output conditions [25]. Narrower bandwidths are needed for low signal-to-noise (SNR) ratios and result in larger integration periods, thereby, retarding response times. These delays were first noticed during duty cycle modulation with results of different sweeping frequencies shown in Figure 26 and were able to be reproduced in Simulink simulations shown in Figure 27. The hysteresis results from low-pass filters within the lock-in amplifier circuits. In the experimental and simulated circuits below, a switching frequency of 100 times the experimental frequency was used to produce similar results in simulation. This difference is due to the number of filters that the signal must pass through and the attenuation values used in the filters. In the simulation, only one low-pass filter was used, whereas the lock-in amplifier used two low-pass and a band-pass filter in the specific output used. Mathematically, the hysteresis may be computed using a convolution of the low-pass filter and the signal using Equation 16 with *h* representing the filter and *x* the input signal (although the variables may be reversed without affecting the result). Figure 28 shows the graphical convolution and plotted results from MATLAB using this function to demonstrate the observed hysteresis which can be predicted by knowing how many pulses the filter will integrate and how fast the duty cycle can change.

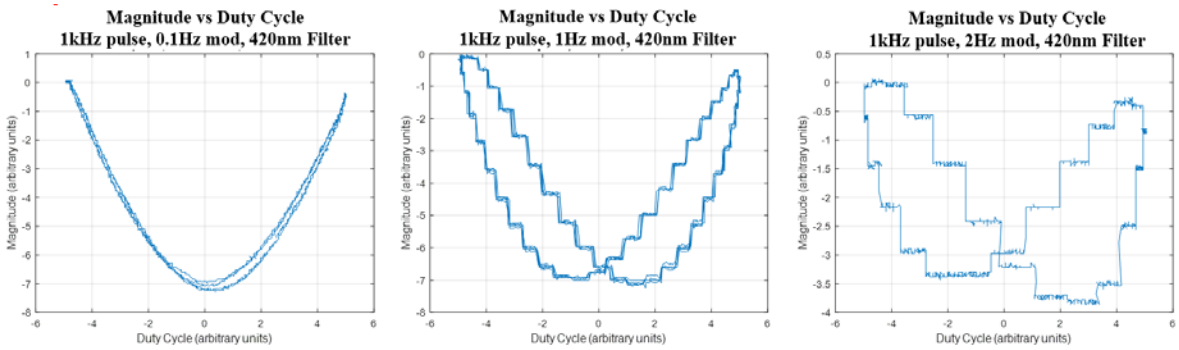

The three graphs above demonstrate the increase in hysteresis as changes in duty cycle increase. Data here was taken from the magnitude output of the Princeton Applied Research SR5210 amplifier to match the magnitude outputs of the simulation which allows for compensation of the output even with a phase shift. However, the granularity of the magnitude output, as seen here, made it unsuitable for calibration.

Figure 26. Observed experimental hysteresis.

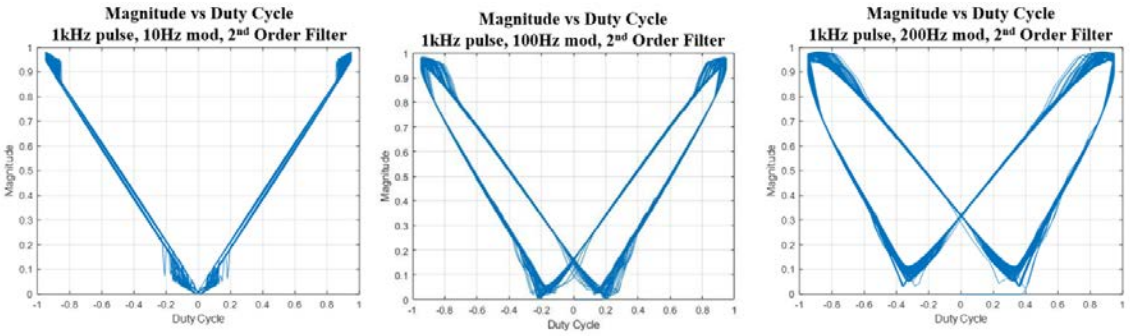

Figure 27. Simulated hysteresis.

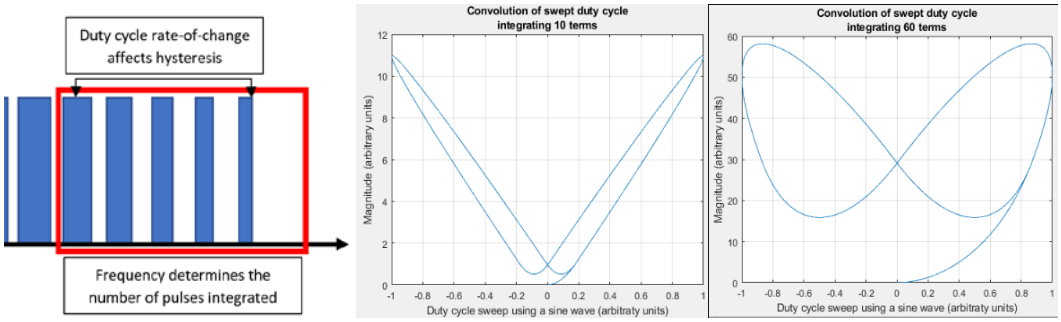

Figure 28. Graphical convolution and results showing hysteresis.

$$y[n] = x[n] * h[n] = \sum_{k=-\infty}^{\infty} h[k]x[n-k] \qquad (16)$$

The replication seen in Figures 27 and 28 above used nearly full sweeps of the duty cycle. In applications where the buck converter seeks to produce a DC output, changes to the duty cycle would be limited with no expected change under a steady load and with only quick shifts of relatively minor changes to the duty cycle for the adding or loss of minor loads. Even in the event of a major load, provided the load is not cycled on and off of the circuit repeatedly, changes in the duty cycle would only require an increase or decrease to a new steady state. In both instances, the difference is the rate or slope of the response which, if the slowest possible rate remains within acceptable parameters, requires no need of duty cycle prediction compensation. Furthermore, if the hysteresis does result in unacceptable changes, the need for mathematical calculations may be avoided if the switching speed can be increased. This is due to the ratio-like relationship between the pulsed frequency and the rate at which the duty cycle is changed. Consequently, increasing the switching frequency decreases the hysteresis if the rate of change in duty cycle is unaltered.

V. DSP/MICROCONTROLLER APPLICATION

Moving to a fully digital signal processing (DSP) setup offers greater flexibility with processing and control development of this novel feedback process. The ultimate goal would be a DSP package that would encompass the processing of the lock-in amplifiers and switching control for a buck converter. As an added benefit, this package would be a general adaptable system, which could easily be adapted and applied to the use of SiC devices used in similar applications. This chapter will discuss the Texas Instruments (TI) F28378D LaunchPad microcontroller unit (MCU) and progress made in utilizing the microcontroller in performing the lock-in amplifier and data processing functions of the light emission system, in addition to integration into the buck converter application.

A. THE TI F28379D MICROCONTROLLER

The TI F28378D MCU is a member of the TI C2000 Delfino series of microcontrollers. Unlike the general purpose field programmable gate array (FPGA) controllers, the C2000 series is specialized for control power applications, specializing in control algorithms and in the use of its peripherals to include 12/16-bit ADCs and ePWM, and three phase controls [32]. In particular, the F28379D (Figure 29) unit contains a dual-core Delfino processor and dual control law accelerators (CLAs) that allow for floating point processing and running speeds up to 200MHz, with each processor core and CLA capable of processing 200 million instructions per second (MIPS), up to one MB of flash memory and 204 KB of RAM [32], [33]. Programming of these units can be accomplished using the TI Code Composer Studio (CCS), although there are other software programming environments which are able to compile code for this C2000 microcontroller. One such third-party software (Simulink) was selected for this project because of familiarity with the software even though it may not be optimal for the operational speed of the microcontroller. Albeit, operational speed will be needed in the final implementation of this system; current needs have focused on the demonstration of operability; hence, optimization will be left for future research.

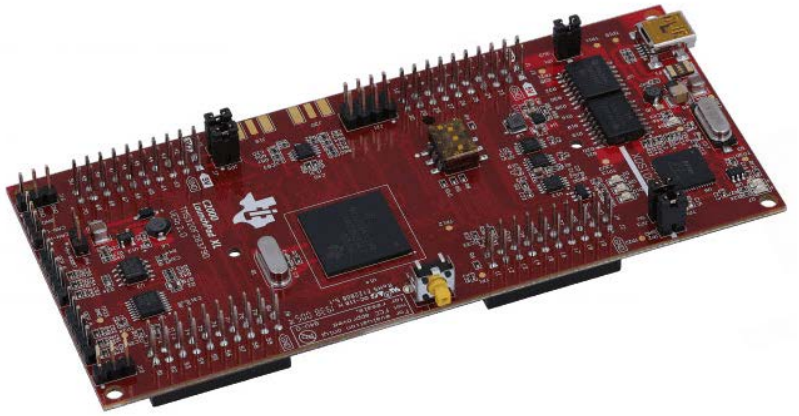

Figure 29. Texas Instruments C2000 F28379D Delfino Microprocessor.

B. MICROCONTROLLER TESTING AND INTEGRATION

With simulations of the lock-in amplifier already created in Simulink for hysteresis analysis, the ability to use Simulink as a programing language made for a simple transition to simulated testing with the MCU. This transition also allowed for multiple options in selection of the reference waveform to use with the lock-in amplifier code, as well as the ability to now consider integration of code for the buck converter switch control into in MCU. These options offer variety in setting how much of the signal of interest will be amplified and then attenuated for the rest of the signal, which can even be further refined with changes in the duty cycle of the reference signal. The only drawback with changes in duty cycle are the need to maintain a near phase-lock between the peaks of the signal of interest and sine or cosine phase reference. The lock is needed to ensure maximum amplification of the signal if the component output is being used. Selection of the magnitude output would avoid the need of syncing phases. Calibration data collected up to this point had been from the sine and cosine outputs of the Princeton Applied Research SR5210 amplifiers due to the granularity of the magnitude output as seen in the data collected for Figure 26. This inability to utilize the magnitude data meant all calibration and testing was based on the component (sine or cosine) outputs, but highlights another advantage of the microcontroller application.

The latest efforts toward use of the microcontroller have focused on completion of a simulated light emission analysis and prediction system. The system will be integrated with a simulated buck converter and switching controls for initial proof-of-concept via Simulink and follow-on testing to be conducted via the F28379D MCU. Unfortunately, one obstacle to the completion of this simulated system has been to adapt the MATLAB code used to predict current and temperature for Simulink—specifically, the "fsolve" function used in MATLAB to backwards calculate current and temperature using the lock-in outputs and calibration polynomials created errors while attempting to compile and load onto the MCU. The work-around created consisted of an interpolation function using two loops to make these predictions. To limit the number of iterations run by the loops, the function uses the desired current of the switch controller and previous temperature predictions to limit the parameters of the two variables within the loops. Simulations using ideal lock-in amplifier inputs allow the narrowing of these parameters to speed up the interpolation process. However, simulated testing with the use of the more realistic lock-in amplifier outputs have required widening the parameters and smaller increments in evaluations that have expanded the amount iterations needed to produce reliable predictions. Of interest, narrowed parameter settings and larger iteration steps used with ideal setting still yield accurate temperature predictions with the unsteady lock-in amplifier inputs. Simulation current predictions tend toward the lower end of the evaluation band, with this tendency lessening as the iteration steps of the temperature are decreased. Accuracy of the current predictions vary with the size of the steps used between iterations and tended to be greater than the >1% error assessed in experimental testing with the physical lock-in amplifiers. Code for the prediction function using polynomial coefficients for the 420 nm and 380 nm can be seen in Appendix C.

Simulation testing of this interpolation prediction function, while not optimal, was possible in Simulink. Starting with use of an ideal input from the lock-in amplifier to the function, both the generated input signal and prediction function used 5^{th} order polynomial coefficients obtained from previous 420 nm and 380 nm experimental calibration results. First was the modulation of current and temperature independently, which tracked as expected for both variables (Figures 30 and 31).

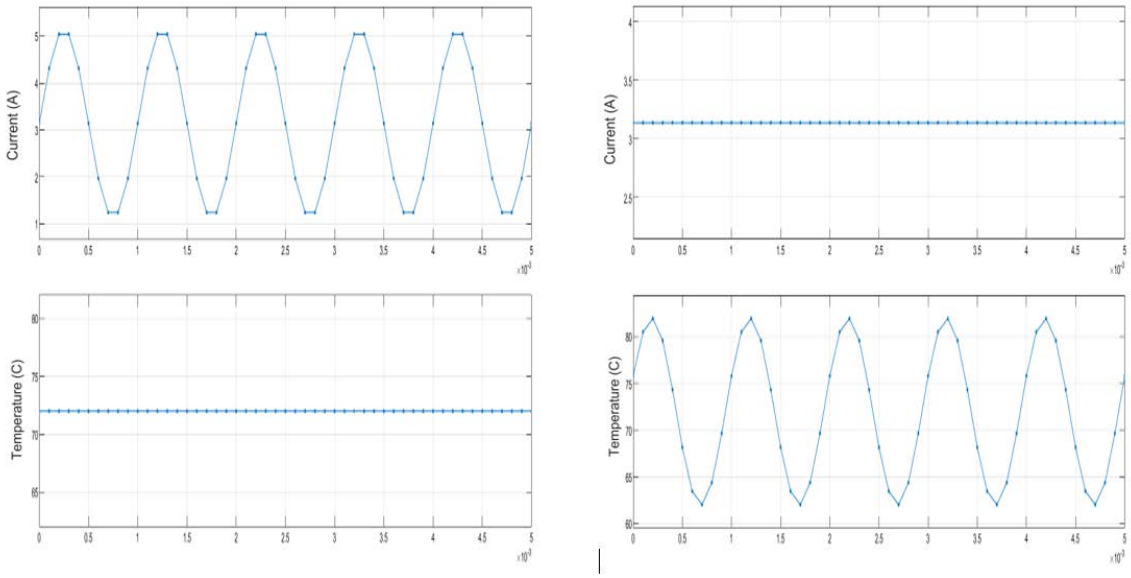

Figure 30. Current and temperature modulation via Simulink.

Testing of the solver on the MCU allowed for narrowing of many of the calculation parameters to speed up the interpolation. In Figure 31, modulation of current and then temperature was performed in the TI F28379D controller. Figure 31 starts with the connection to the ideal outputs being connected, modulation of the current is then followed by modulation of the temperature, and finally both variables are modulated simultaneously. Highlighted in red boxes are areas where modulations of the temperature affected current predictions, which was also observed in experimental test shown in Figure 21. Furthermore, the noted jump of 0.2 A corresponded to the current iteration step size used in the interpolation, meaning that the function was able to find an acceptable solution at exactly one iteration sooner. Smaller iteration step sizes were able to lessen these fluctuations, but at the expense of speed within the solver. Modulation of the current, even with simulated 70 A oscillations, made no changes in the predicted temperature—suggesting temperature as the dominate variable in this range and filter selection.

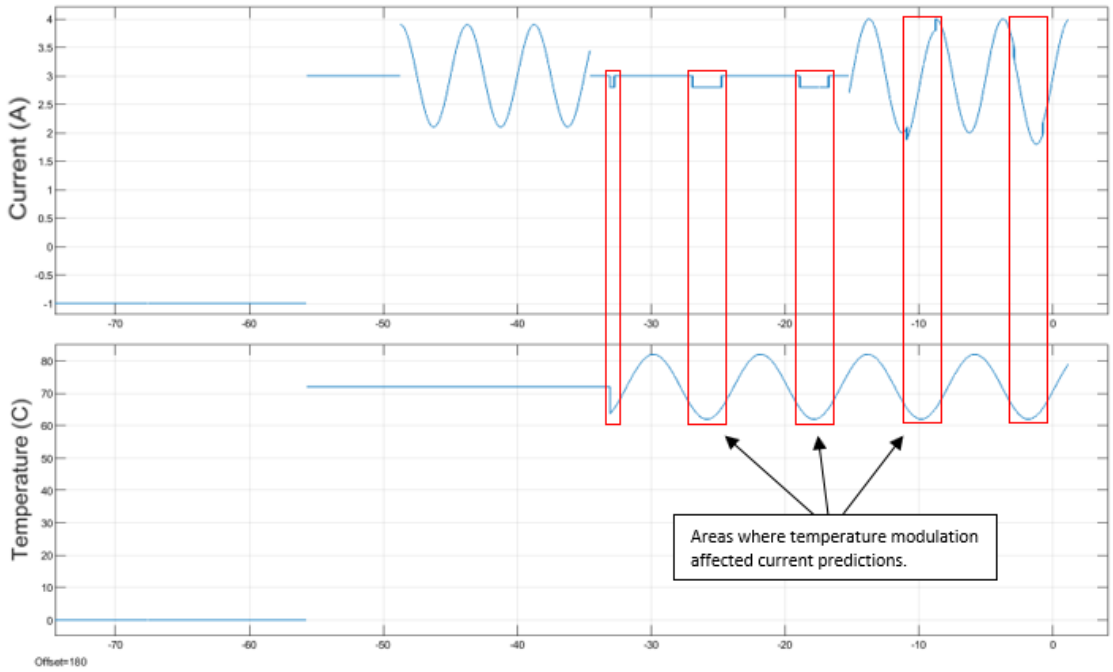

This figure depicts testing of the current and temperature prediction function running on the TI F28379D LaunchPad MCU. Highlighted by the red blocks, affects in current predictions can be seen with modulation of the temperature which was also observed in the experimental testing.

Figure 31. Current and temperature modulation via the MCU.

Unfortunately, the interpolation prediction function, while operational, is currently still too slow to be practical for use in the buck converter application. Narrowing of tolerance bands and increasing of the iteration steps does speed up the process, but will likely not be enough improvement to reach the desired output rates. Considering options to address the speed impediment of this function, the most plausible would be to change the programming software to Code Composer Studio or Energia IDE. Since these programs are specifically designed for the programming of microcontrollers, their compiled code is likely to be much less cumbersome with quicker execution. Another consideration would be to investigate into if either of these programs contain a built-in Newtonian-like solver capable of handling the multivariable polynomials of this research. In the event the code cannot be optimized to reach required prediction speeds, transmission of the lock-in amplifier outputs to an external source via the USB connection for prediction analysis is also possible. Although, external processing should be discouraged until other options have

been explored. The concern is real time communications would also likely bog down the MCU processors, not to mention added time for transmission, and the use of external devices for prediction calculation involve increased cost and complexities in the system.

VI. CONCLUSIONS AND FUTURE WORK

This research demonstrated photonic emissions from a GaN vertical diode can successfully be used to determine current and temperature of the device. However, a number of considerations need to be addressed for this method to be integrated into the control feedback loop of a power system. These considerations will be discussed in the following conclusions and will be followed by thoughts on addressing or improving these areas in the future work section.

A. CONCLUSIONS

This research focused on the light emissions from a Gallium Nitride diode, using optical filters of 370 nm, 380 nm, 390 nm, 400 nm, 420 nm, and 550 nm. Testing parameters consisted of a current range from 0.5 A to 4.0 A, temperatures from 20 °C to 100 °C, frequencies up to 1 kHz, and duty cycle modulation.

The quality of predictions of current and temperature depends on the accuracy of the calibration surfaces and corresponding polynomial coefficients. Consequentially, prediction accuracy is also highly dependent on the filters used and the operating parameters of the device. Selection of filters will differ based on operating current and temperature to ensure photodiodes being excited by the photonic emissions are able to detect changes within the desired range. Filters selection should also be biased to those around the 370 nm and 390 nm peaks due to these emissions being directly related to the GaN. However, testing results demonstrate wavelengths in vicinity of the 420 nm and 550 nm peak can be used, but further testing of these two peaks is needed to determine the effects of these impurity produced emissions over time. For devices which will operate under a wide range of currents of temperatures, addition of a third or fourth optical filter may be needed. The use of optical filters with wider passbands may satisfy use in more limited ranges. Either option would help to ensure the shifting of the emission peaks during current and temperature variations would not exceed the bandwidths of the filters. Calibration also needs to be conducted on the full expected operational current and temperature range of the device, since the values of polynomials generated in the

calibration cannot be expected to follow the actual response of the device outside of the mapped surface used in the calibration process. Finally, decisions may have to be made of the required accuracy of the system and available processing power since higher order polynomials may be able to provide a better fit; but are likely to prove more costly in needed processing power and in time needed to calculate predictions. An external computer may perform these calculations, but there is a concern that extra processing power is needed by the MCU for real-time transmissions in addition to any delays in transmission times to and from the external source. Use of an external calculation source also diminishes cost savings obtained with the purely microcontroller application.

The initial testing setup may prove adequate in higher current GaN applications; however, the ultimate desire is for this process to be applicable in broader range of applications such as low power and with power devices using materials with much lower photonic emissions like SiC. Since the broader application will deal with much weaker signals, resorting to the use of the lock-in amplifier provides a logical solution. The lock-in amplifiers also presented new challenges. The Princeton Applied Research SR5210 lock-in amplifiers used in this testing limited frequencies to 120 kHz or less [25]. Future applications will require the use of a newer lock-in amplifiers or microcontrollers for the capacity to process higher frequencies [25]. Finally, hysteresis effects occurring from the use of low-pass filters will also need to be accounted for when rapid response speeds and large changes in duty cycle are desired.

B. FUTURE WORK

As with any developing technology, much work is needed to move these findings into practical application. Known areas that have not yet been explored or which require more research for optimization are now discussed.

1. Range and Stability Testing

Testing of the photonic emissions of GaN has, up to this point, only been conducted in a narrow range at the low end of general power converter applications. Initial spectrometer analysis of the DUT was conducted up to 1 A and 120 °C. This research has now expanded the current testing up to 4 A, but desired power systems have applications

than maintain currents of several hundred amperes. Mapping of photonic emissions through these higher operating currents and to greater temperatures are needed to fully understand the emission response of the device. Knowing the full extent of the emission peak shifts would aid in filter selection and associated parameter requirements such as bandwidth.

Long term degradation testing is also needed to determine if and how the photonic emissions will change over the life of the device. Data would then be used to determine how often recalibration is needed and if recalibration requirements are dependent on the emission peaks being utilized. The primary interest in comparing the different emission peaks is to determine if light emission peaks from impurities within the device are stable enough to be used for life of the device. Furthermore, the trend analysis from this data would be expected to help in predicting device degradation.

2. Optical Coupling

Referring back to diodes in Figures 3 and the right image in Figure 13 of light emitting from the GaN diode, photonic emissions are created at the PN junction of the device. In a LED, this junction is placed near an open edge on the device to facilitate the escape of photons from the device. As shown in Figure 3, this is not the case with power electronic devices, where the PN junction is located under a terminal connection and photonic emissions must travel through the body of the device, where they are absorbed and re-emitted and internal reflection diminishes the actual light emission from the device at multiple points. Noting the optical fiber on a single side of the device and light emissions from all sides in Figure 13, the estimated collection of light by the cable when compared to the total light emissions is, at best, less than 40%. Strength of the collected emissions are diminished even further by gaps, between the fiber end and filter as well as between the filter and photodiode, allowing further loss of light. Narrowing these gaps during testing resulted in a two- to four-fold increase in the photodiode output. It is assessed that increases in the light emission capture at the device would also yield substantial signal increases. Additionally, emission output from the power diode may also be improved by adding an

area for photonic emissions to escape and be directed into an optical fiber— provided this can be accomplished without substantially diminishing any other properties of the device.

3. Junction Temperature Calculations

Temperate readings from outside a device are common. However, the strength in temperature predictions via photonic emissions is that the predictions are near real-time vice delayed responses from an external probe. Since time required for heat transfer between the PN junction and the probe, these delays can be substantial and can result in unmeasurable change at the probe. Additionally, in decreasing current of temperature situations, the location of the probe is also limited by the ability to dissipate heat in that particular location. To make these junction temperature predictions, heat transfer coefficients from the PN junction, where the heat is generated, to the location of the temperature probe need to be calculated. Knowledge of the junction temperature will help identify optimal device operation and can be used to identify device degradation.

4. DSP/Microcontroller Solutions

The desire to shift to a DSP setup results from the abilities to manipulate and process data offered by a DSP system. Use of a microcontroller is a logical choice as a means of moving toward a DSP solution with built in A2D, digital to analog (D2A), and pulse width modulated (PWM) inputs and outputs, USB and serial communication capability, and internal processing ability. Microcontrollers possess the added benefit of low cost and a history of incorporation into high-speed and industrial applications. Simulink simulations and data sheet ratings suggest the TI C2000 F28379D microcontroller should be able to duplicate the functions of the locked-in amplifier as well as the switching control. However, testing of microcontroller integration has not been fully implemented, and challenges, such as the ability to reverse calculate current and temperature predictions with the calibration best-fit polynomial coefficients, have yet to be fully demonstrated.

APPENDIX A. CALIBRATION SURFACES

A. THORLABS FDS010 PHOTODIODE SURFACES

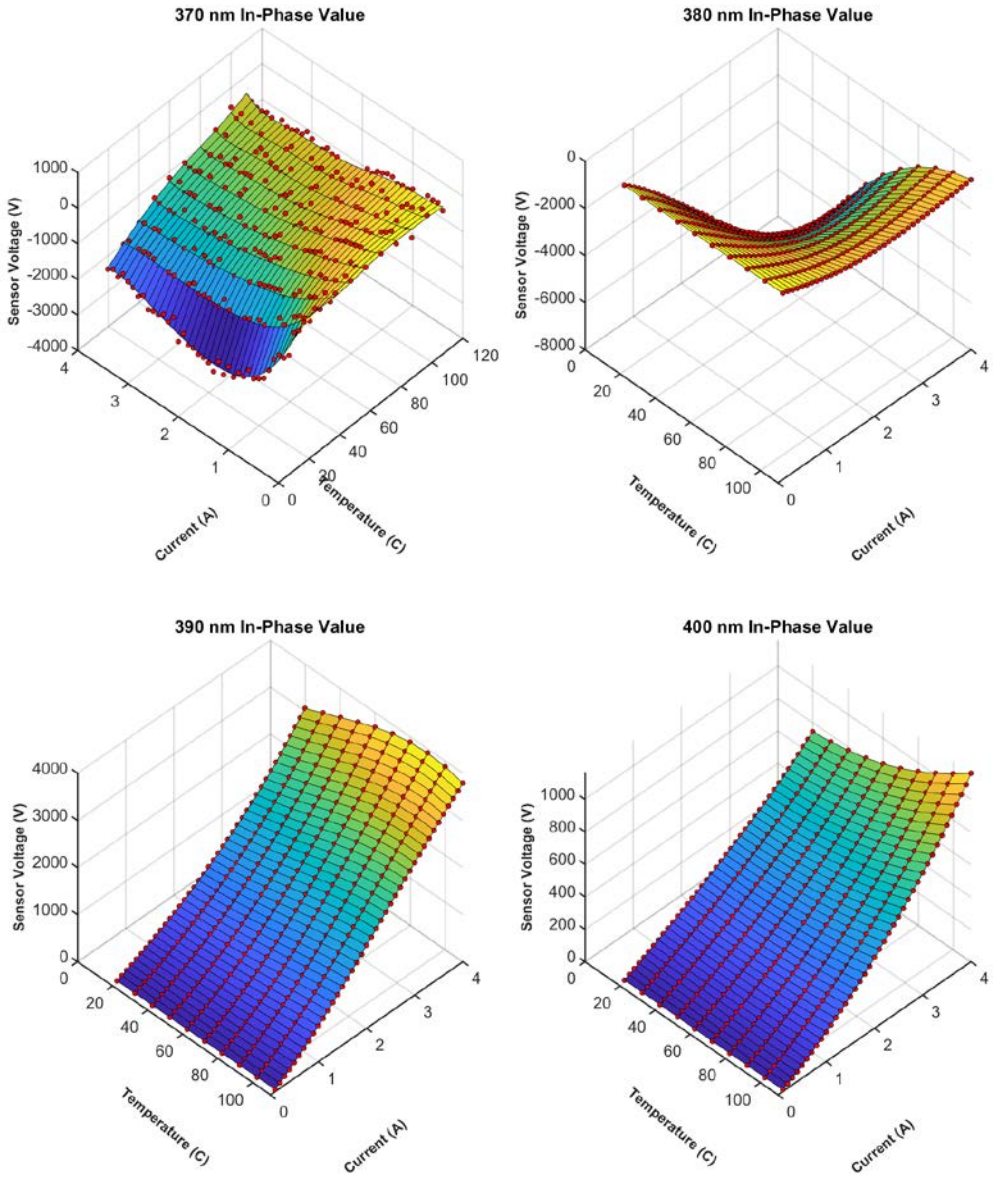

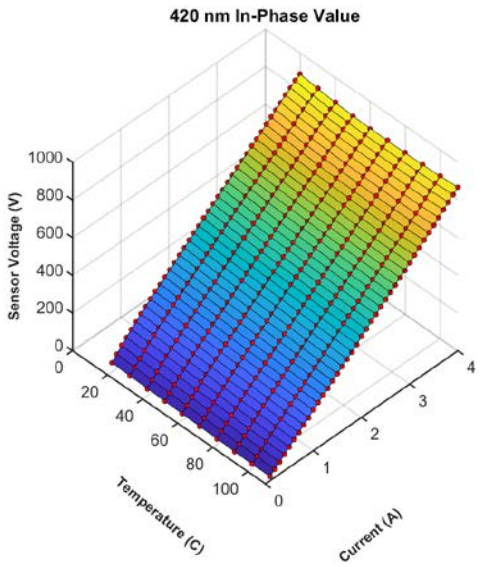
420 nm In-Phase Value
Sensor Voltage (V)
1000
800
600
400
200
0
0
20
40
60
80
100
Temperature (C)
0
1
2
3
4
Current (A)

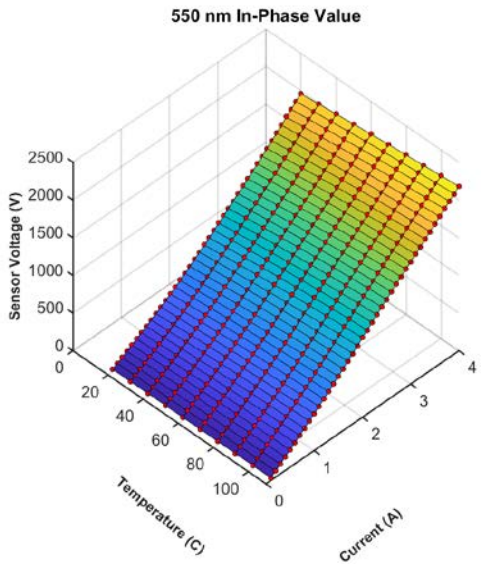
550 nm In-Phase Value
Sensor Voltage (V)
2500
2000
1500
1000
500
0
0
20
40
60
80
100
Temperature (C)
0
1
2
3
4
Current (A)

B. THORLABS APD130A2 AVALANCHE PHOTODIODE SURFACES

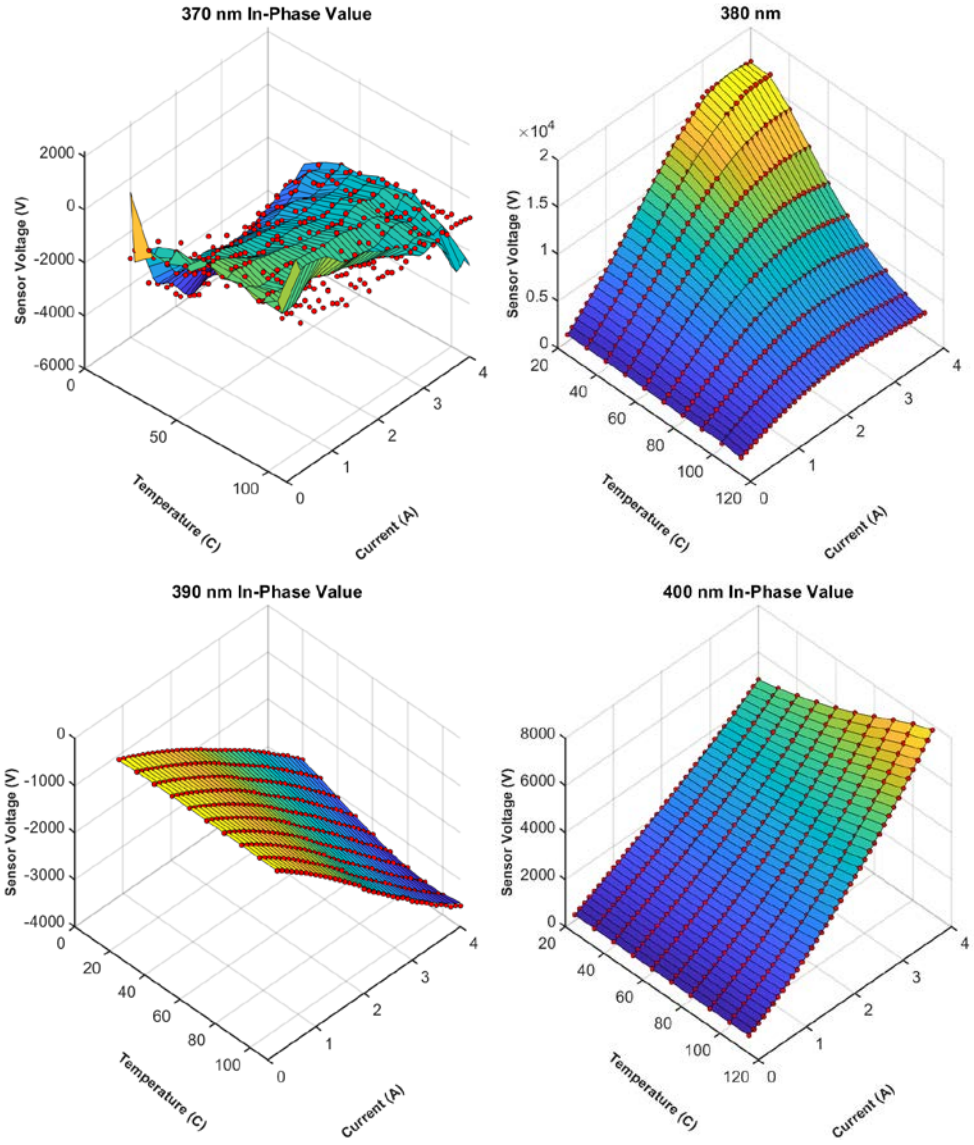

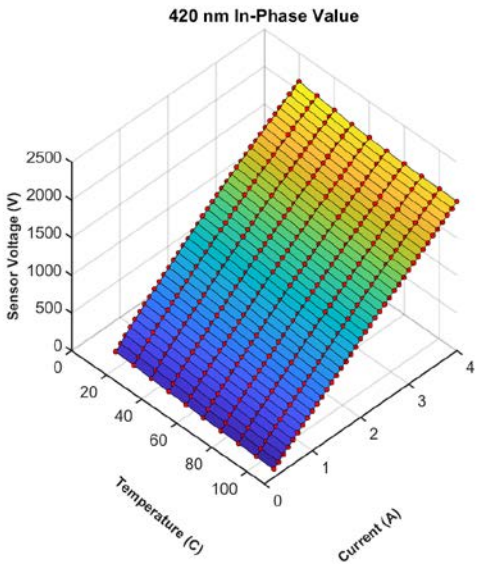
420 nm In-Phase Value
Sensor Voltage (V)
2500
2000
1500
1000
500
0
0
20
40
60
80
100
Temperature (C)
0
1
2
3
4
Current (A)

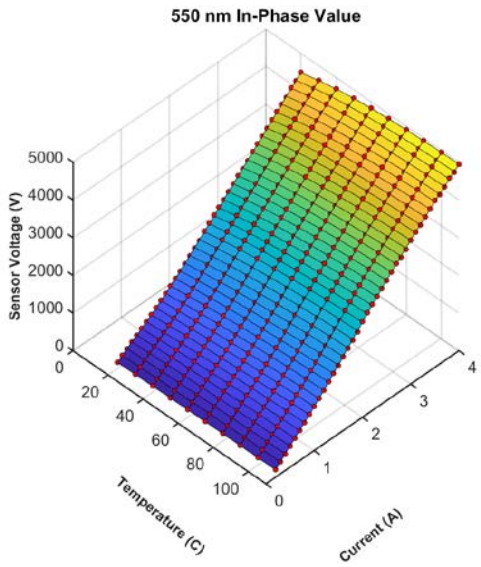
550 nm In-Phase Value
Sensor Voltage (V)
5000
4000
3000
2000
1000
0
0
20
40
60
80
100
Temperature (C)
0
1
2
3
4
Current (A)

APPENDIX B. CURRENT AND TEMPERATURE CONTOURS

The following charts plot the sensor voltage outputs from the calibration surfaces in Appendix A from zero to 4 A and 20 °C to 110 °C. By comparing the outputs of two different filter surfaces, unique crossings of the output voltages can then be used for backward calculations of current and temperature within the range of calibration data.

A. THORLABS FDS010 PHOTODIODE CONTOURS

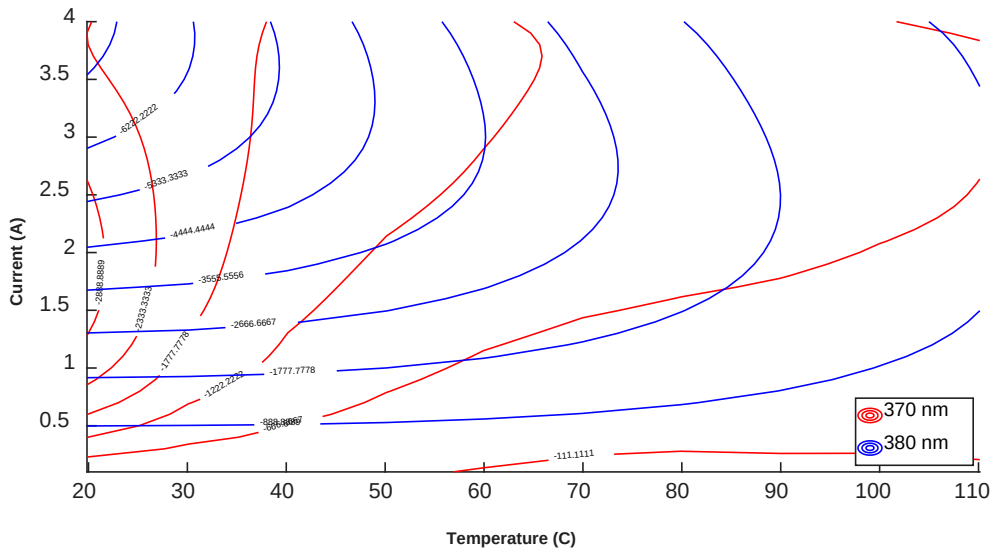

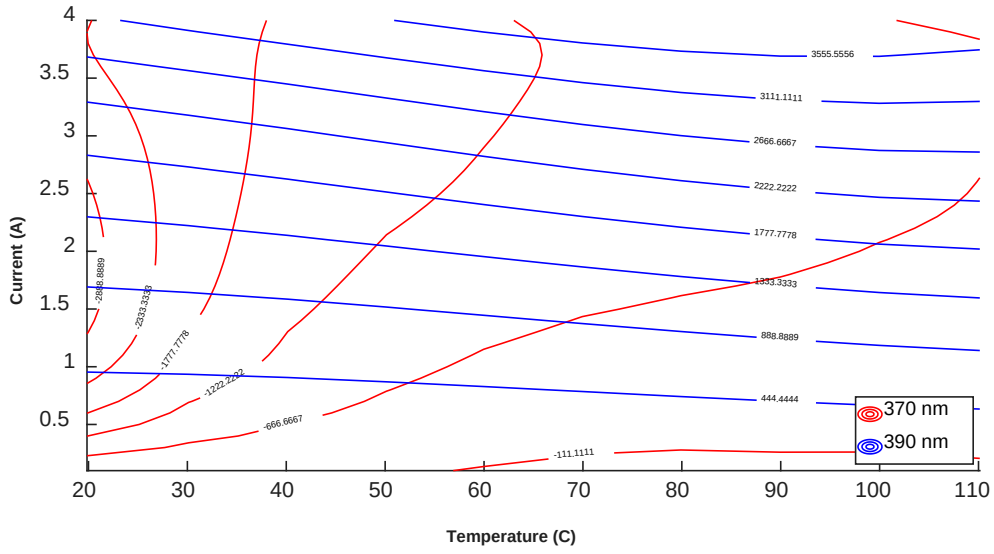

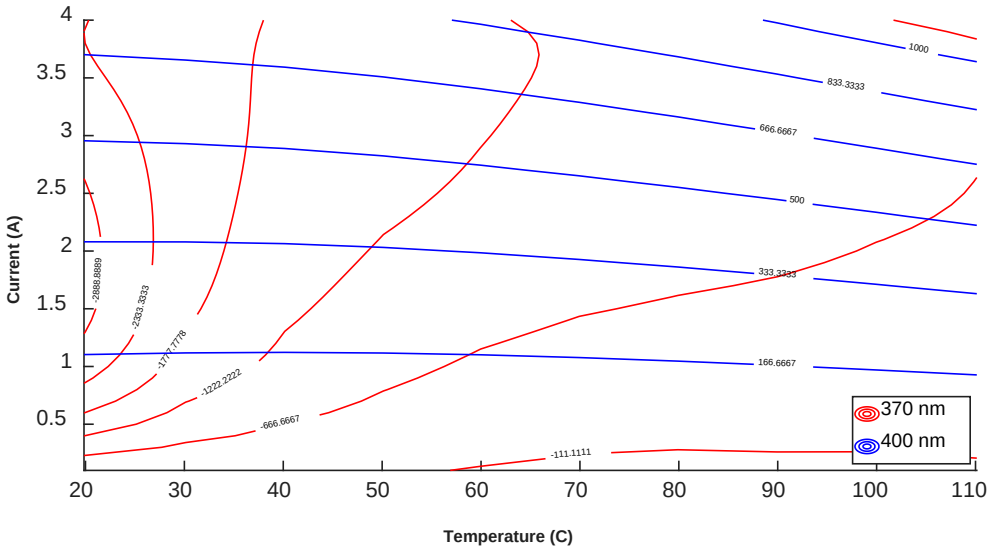
Current (A)
Temperature (C)
1000
833.3333
666.6667
500
333.3333
166.6667
-2888.8889
-2333.3333
-1777.7778
-1222.2222
-666.6667
-111.1111
370 nm
400 nm

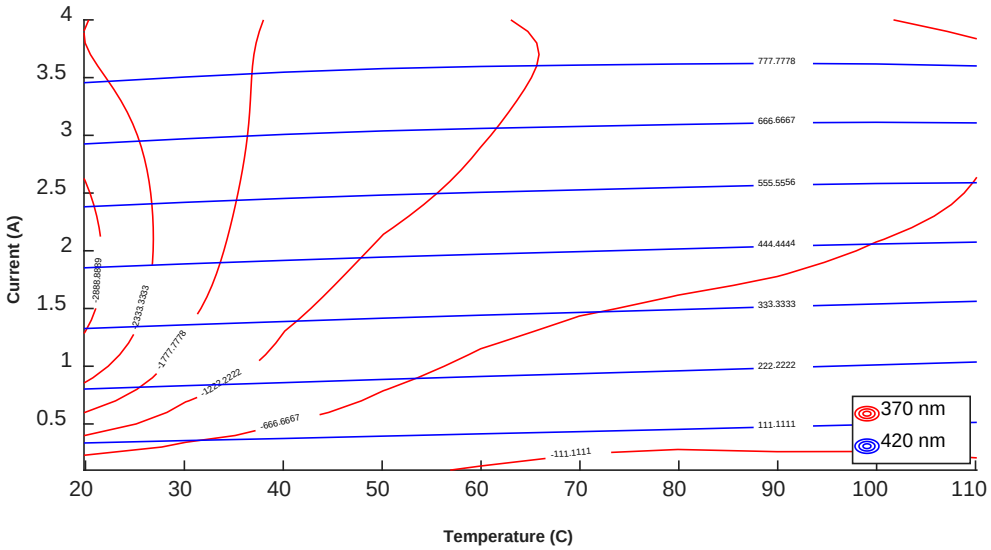
Current (A)
Temperature (C)
777.7778
666.6667
555.5556
444.4444
333.3333
222.2222
111.1111
-2888.8889
-2333.3333
-1777.7778
-1222.2222
-666.6667
-111.1111
370 nm
420 nm

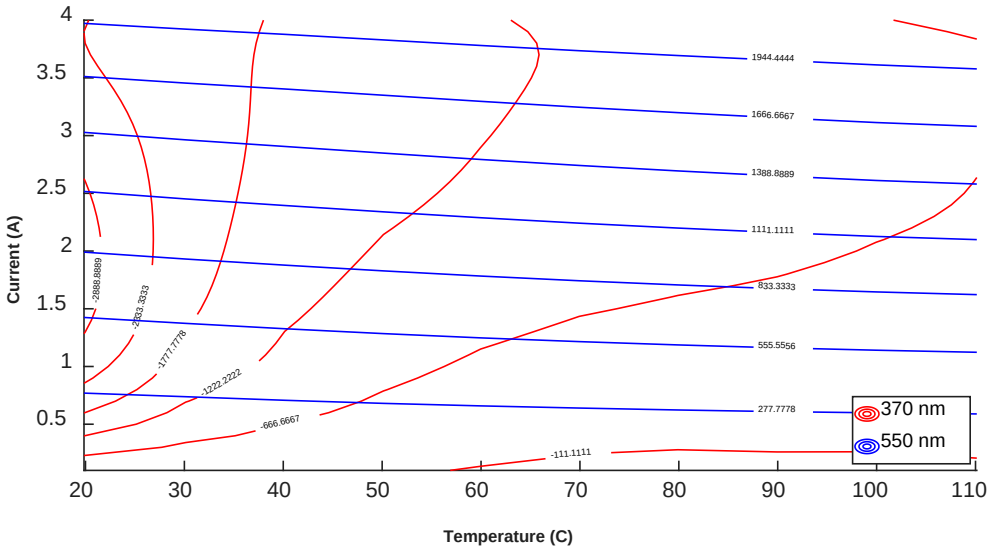
Current (A)
Temperature (C)
370 nm
550 nm
1944.4444
1666.6667
1388.8889
1111.1111
833.3333
555.5556
277.7778
-2888.8889
-2333.3333
-1777.7778
-1222.2222
-666.6667
-111.1111

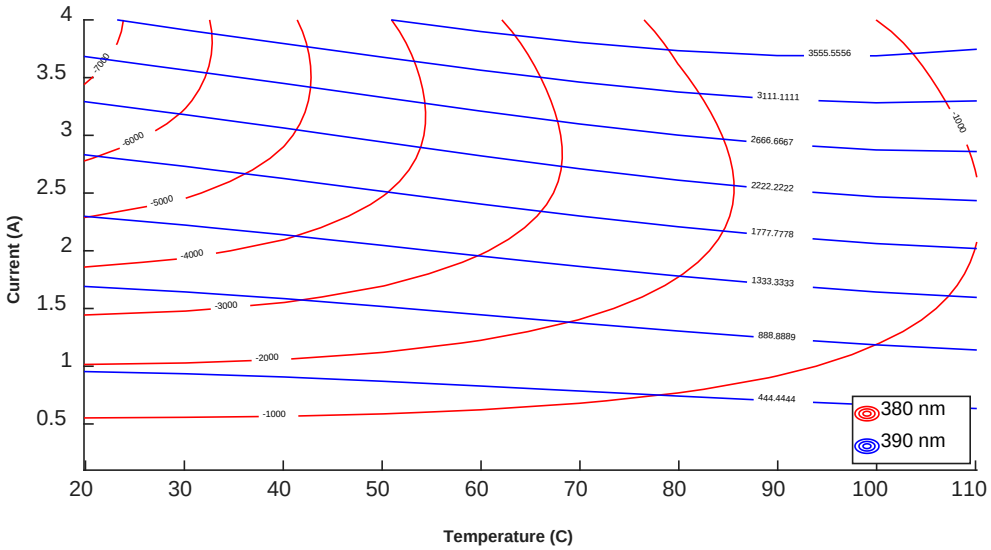
Current (A)
Temperature (C)
380 nm
390 nm
3555.5556
3111.1111
2666.6667
2222.2222
1777.7778
1333.3333
888.8889
444.4444
-7000
-6000
-5000
-4000
-3000
-2000
-1000

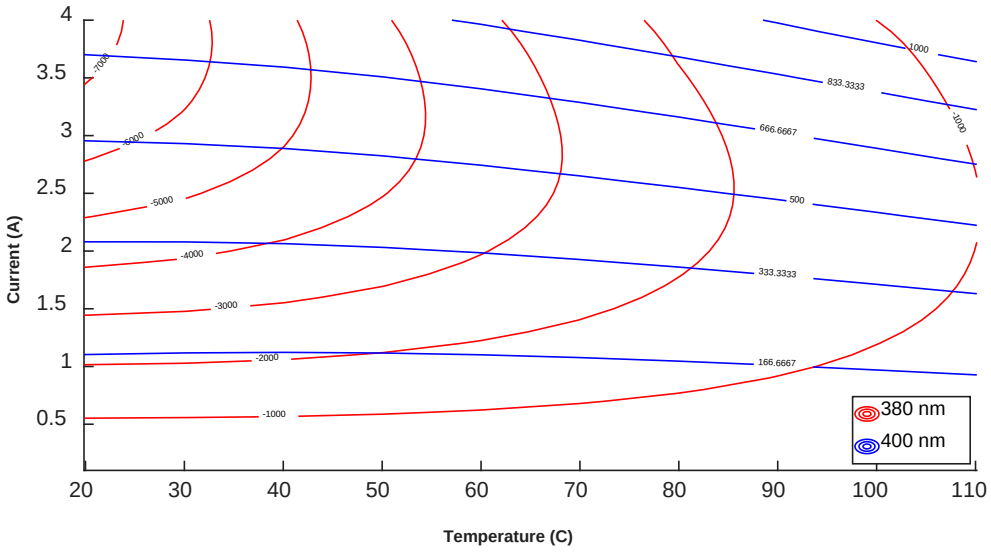
Current (A)
Temperature (C)
380 nm
400 nm
-7000
-6000
-5000
-4000
-3000
-2000
-1000
1000
833.3333
666.6667
500
333.3333
166.6667

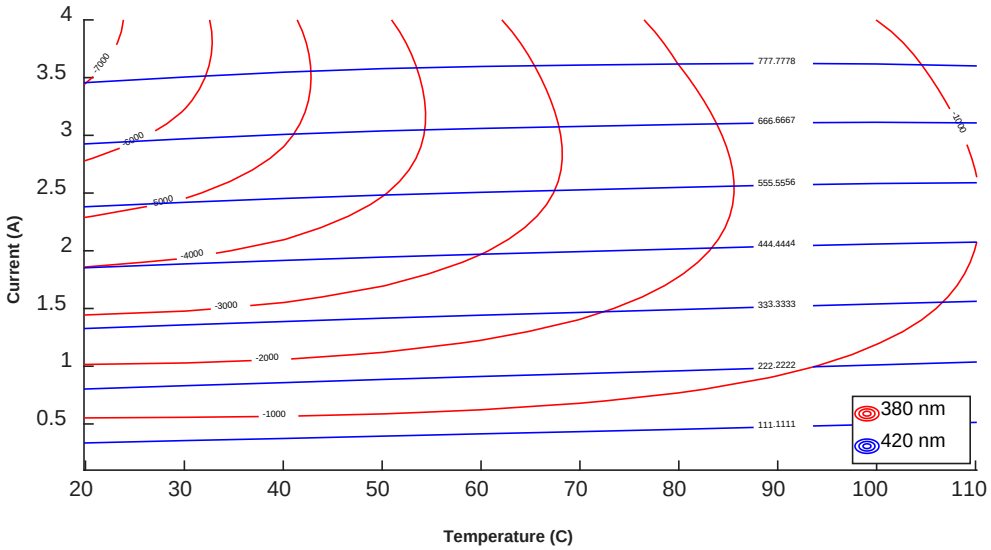
Current (A)
Temperature (C)
380 nm
420 nm
-7000
-6000
-5000
-4000
-3000
-2000
-1000
777.7778
666.6667
555.5556
444.4444
333.3333
222.2222
111.1111

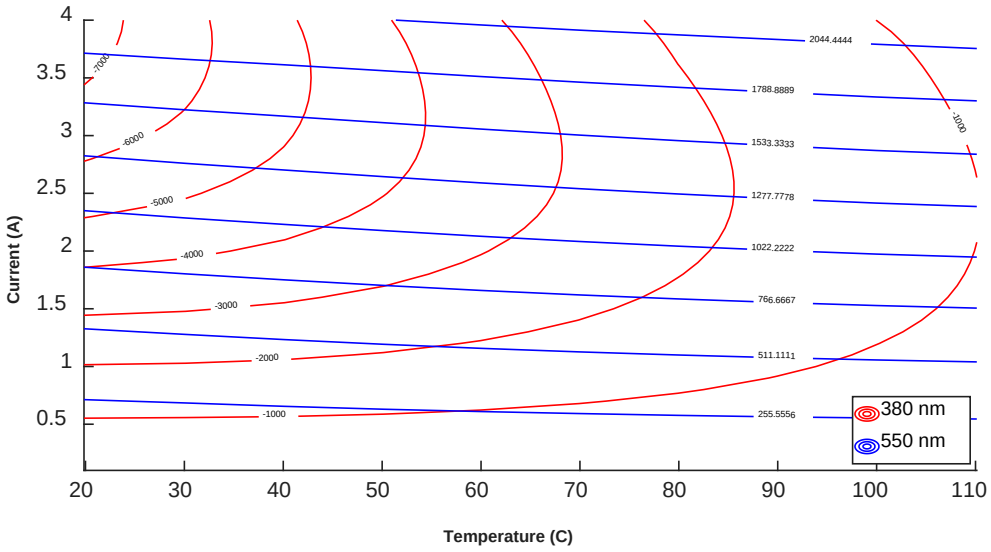
Current (A)
Temperature (C)
380 nm
550 nm
2044.4444
1788.8889
1533.3333
1277.7778
1022.2222
766.6667
511.1111
255.5556
-7000
-6000
-5000
-4000
-3000
-2000
-1000
-1000

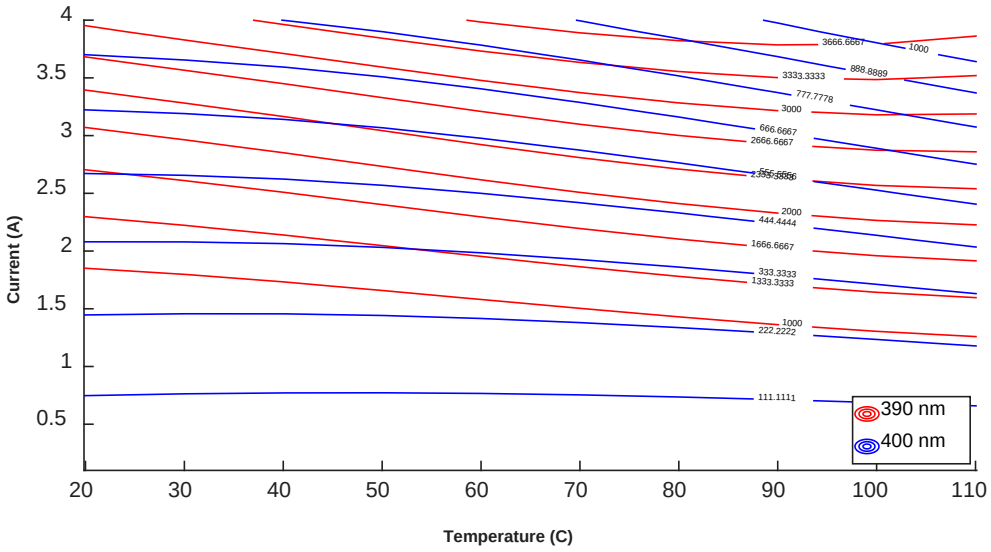
Current (A)
Temperature (C)
390 nm
400 nm
3666.6667
1000
888.8889
3333.3333
777.7778
3000
666.6667
2666.6667
2000
444.4444
1666.6667
333.3333
1333.3333
1000
222.2222
111.1111

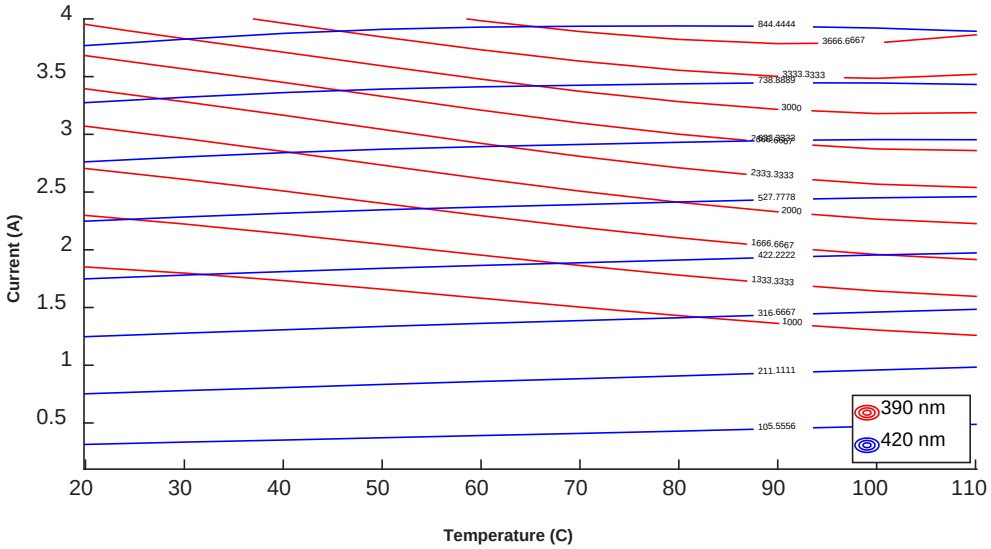
Current (A)
Temperature (C)
390 nm
420 nm
844.4444
3666.6667
3333.3333
738.8889
3000
2333.3333
527.7778
2000
1666.6667
422.2222
1333.3333
316.6667
1000
211.1111
105.5556

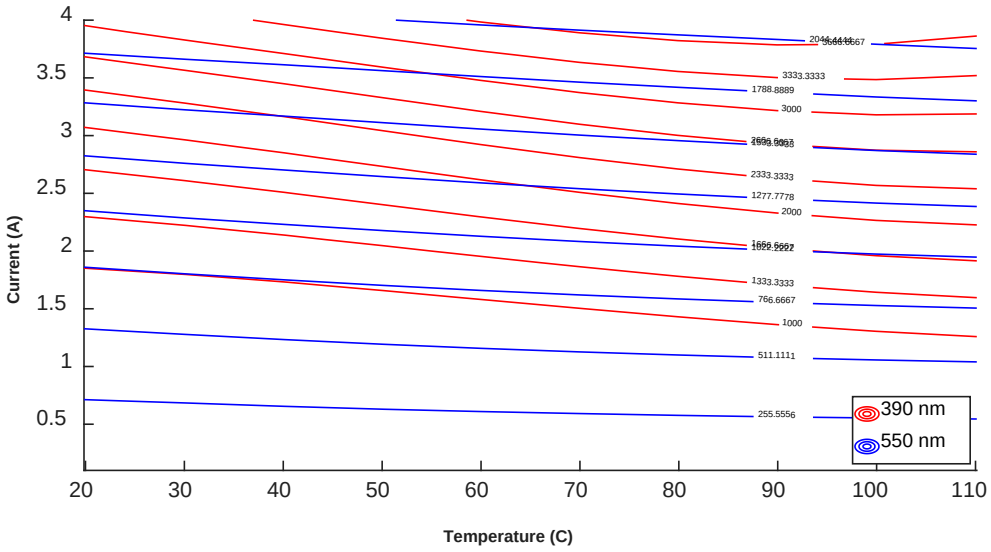
Current (A)
Temperature (C)
390 nm
550 nm
255.5556
511.1111
766.6667
1000
1333.3333
1022.2222
1277.7778
2000
2333.3333
1666.6667
1788.8889
3000
3333.3333

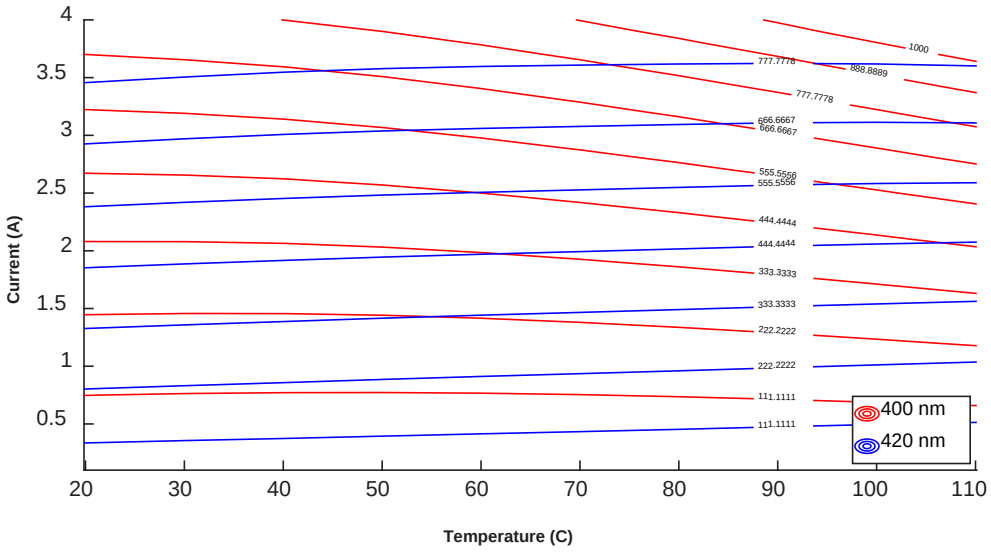
Current (A)
Temperature (C)
400 nm
420 nm
111.1111
222.2222
333.3333
444.4444
555.5556
666.6667
777.7778
888.8889
1000

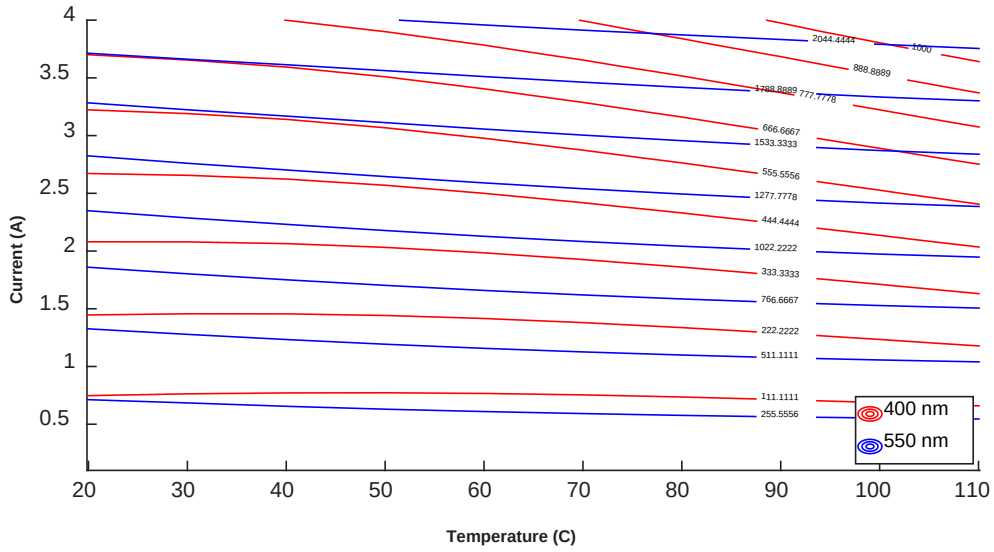
Current (A)
Temperature (C)
2044.4444
1000
888.8889
1788.8889
777.7778
666.6667
1533.3333
555.5556
1277.7778
444.4444
1022.2222
333.3333
766.6667
222.2222
511.1111
111.1111
255.5556
400 nm
550 nm

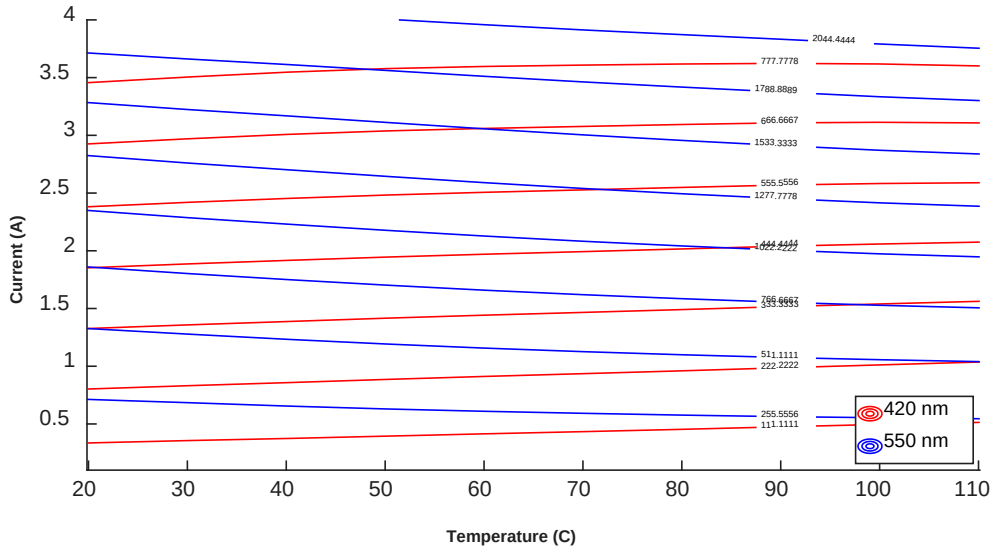
Current (A)
Temperature (C)
2044.4444
777.7778
1788.8889
666.6667
1533.3333
555.5556
1277.7778
511.1111
222.2222
255.5556
111.1111
420 nm
550 nm

B. THORLABS APD130A2 AVALANCHE PHOTODIODE CONTOURS

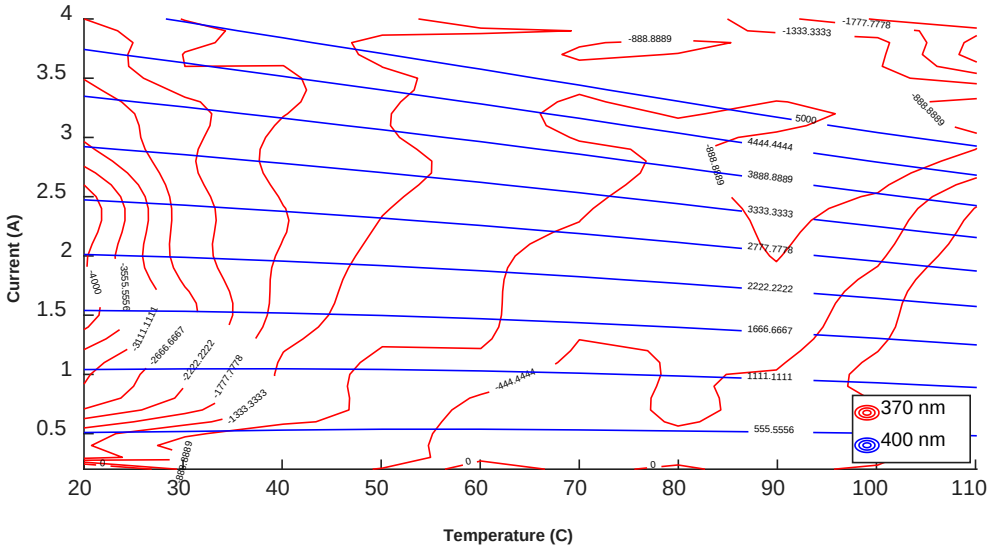

As shown in the 370 nm trace above, to the poor quality of the 370 nm calibration surface and resulting best-fit polynomial would be sub-optimal for reliable predictions. Hence no further contours for the 370 nm filter were ran with the avalanche photodiode setup.

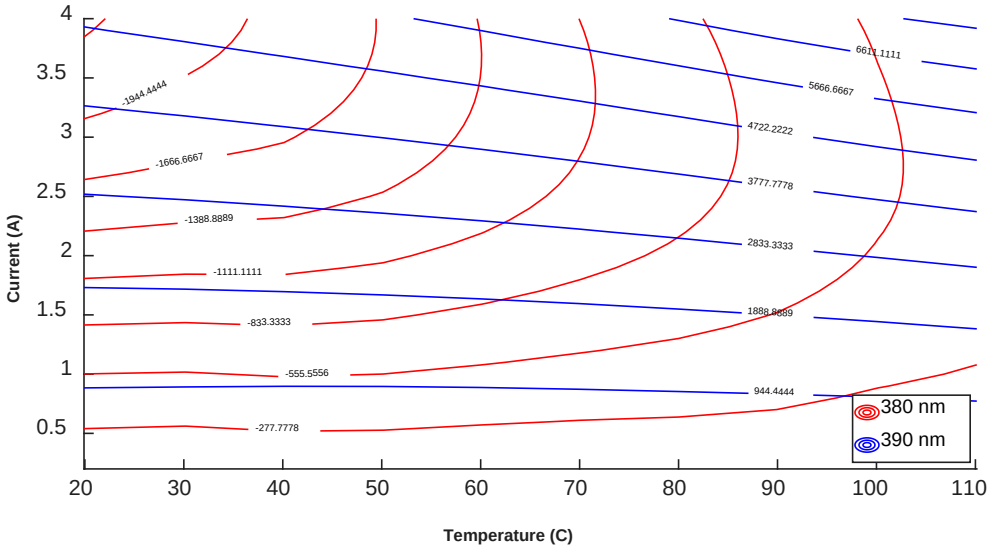

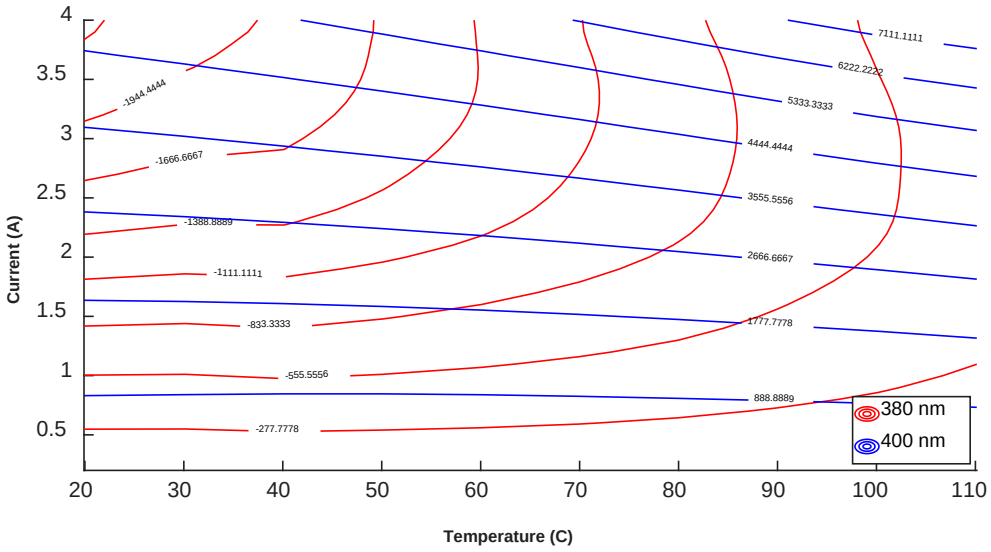
Current (A)
Temperature (C)
-1944.4444
-1666.6667
-1388.8889
-1111.1111
-833.3333
-555.5556
-277.7778
7111.1111
6222.2222
5333.3333
4444.4444
3555.5556
2666.6667
1777.7778
888.8889
380 nm
400 nm

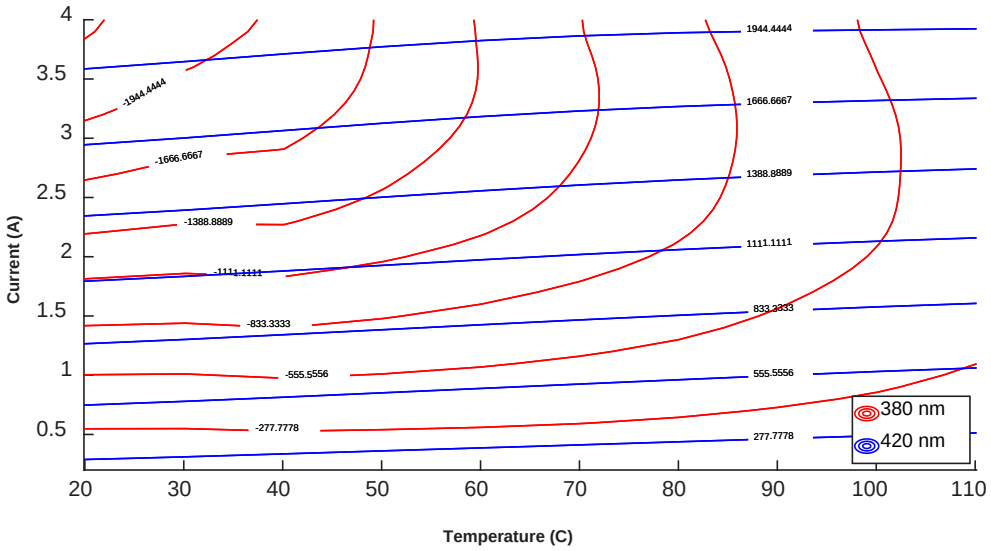
Current (A)
Temperature (C)
-1944.4444
-1666.6667
-1388.8889
-1111.1111
-833.3333
-555.5556
-277.7778
1944.4444
1666.6667
1388.8889
1111.1111
833.3333
555.5556
277.7778
380 nm
420 nm

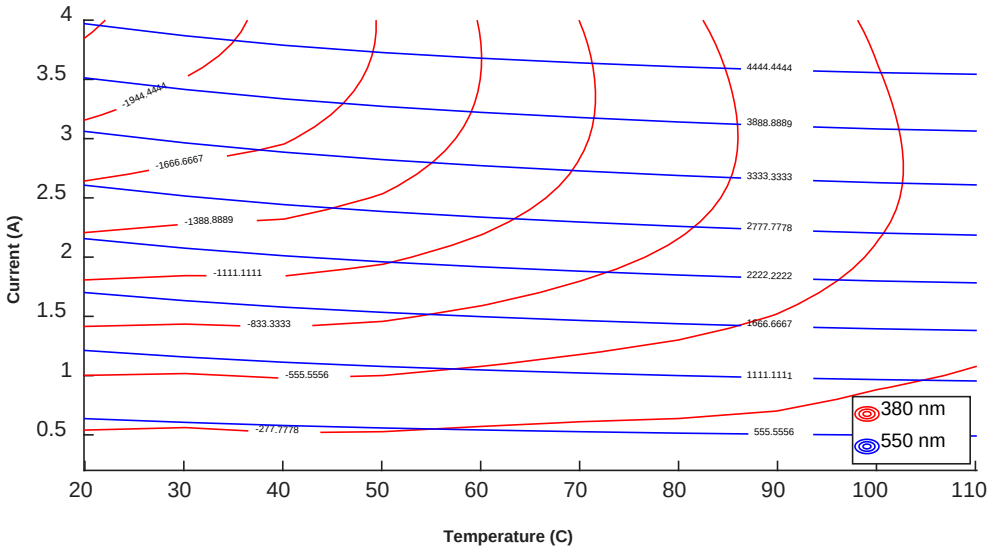
Current (A)
Temperature (C)
4444.4444
3888.8889
3333.3333
2777.7778
2222.2222
1666.6667
1111.1111
555.5556
-1944.4444
-1666.6667
-1388.8889
-1111.1111
-833.3333
-555.5556
-277.7778
380 nm
550 nm

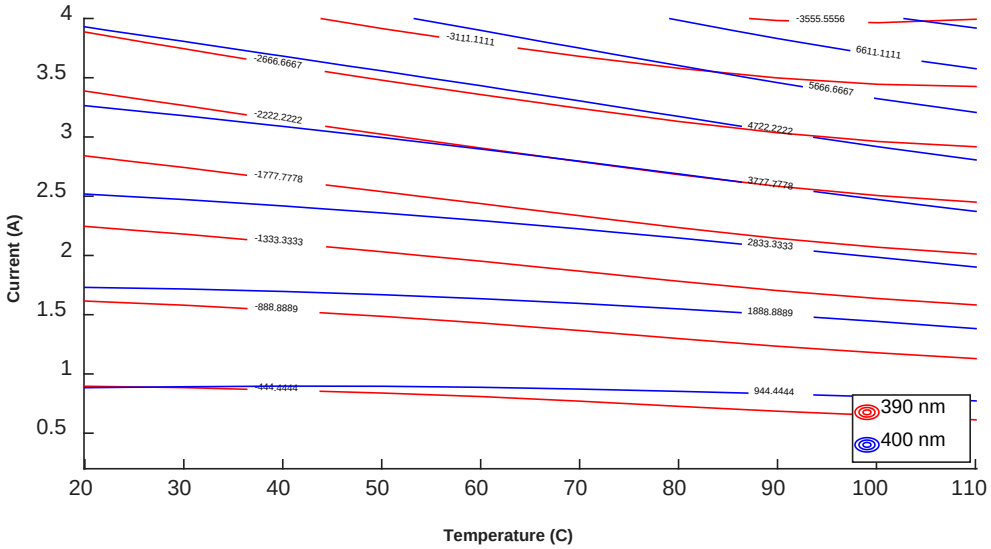
Current (A)
Temperature (C)
-3555.5556
6611.1111
5666.6667
4722.2222
3777.7778
2833.3333
1888.8889
944.4444
-3111.1111
-2666.6667
-2222.2222
-1777.7778
-1333.3333
-888.8889
-444.4444
390 nm
400 nm

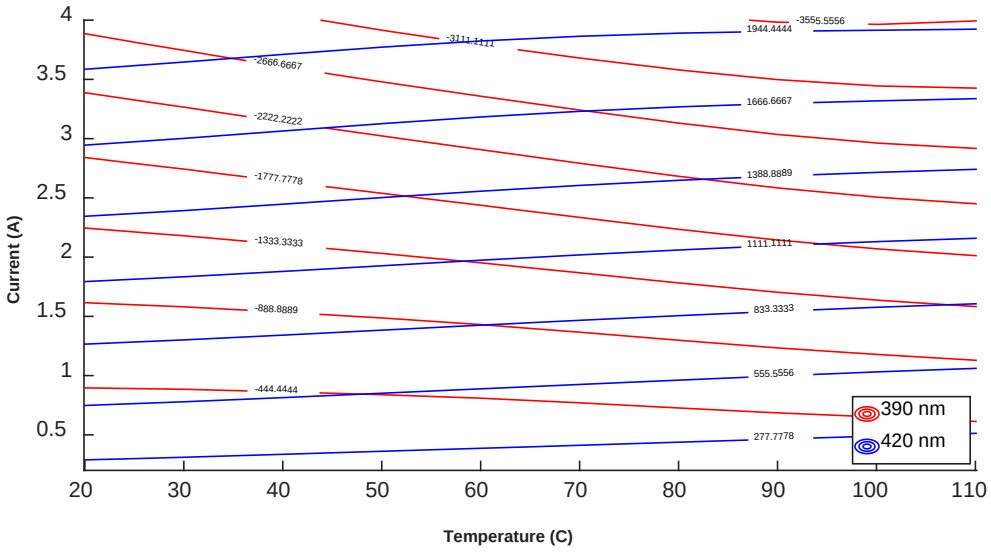
Current (A)
Temperature (C)
-3555.5556
-3111.1111
-2666.6667
-2222.2222
-1777.7778
-1333.3333
-888.8889
-444.4444
1944.4444
1666.6667
1388.8889
1111.1111
833.3333
555.5556
277.7778
390 nm
420 nm

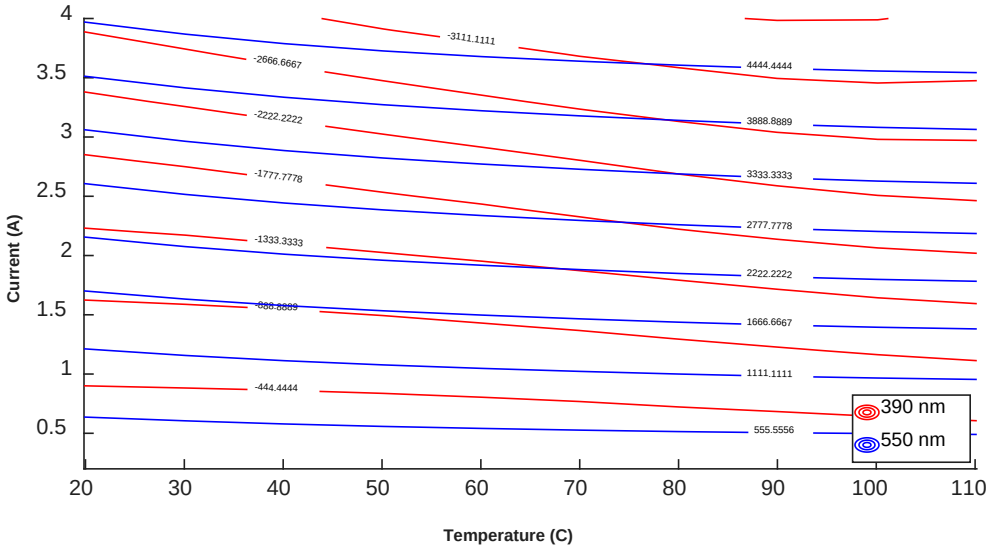
Current (A)
Temperature (C)
-3111.1111
-2666.6667
-2222.2222
-1777.7778
-1333.3333
-888.8889
-444.4444
4444.4444
3888.8889
3333.3333
2777.7778
2222.2222
1666.6667
1111.1111
555.5556
390 nm
550 nm

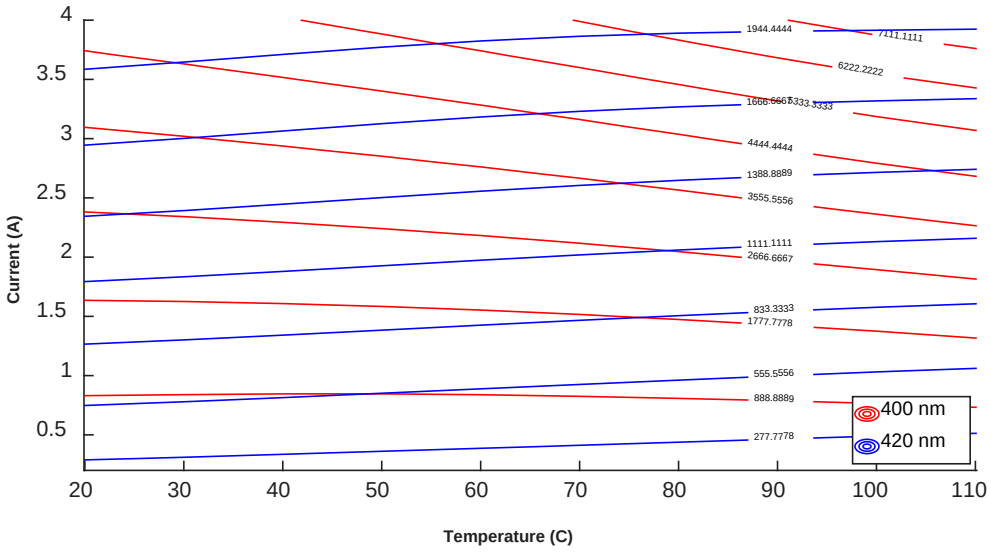
Current (A)
Temperature (C)
400 nm
420 nm
1944.4444
7111.1111
6222.2222
5333.3333
4444.4444
1388.8889
3555.5556
1111.1111
2666.6667
833.3333
1777.7778
555.5556
888.8889
277.7778

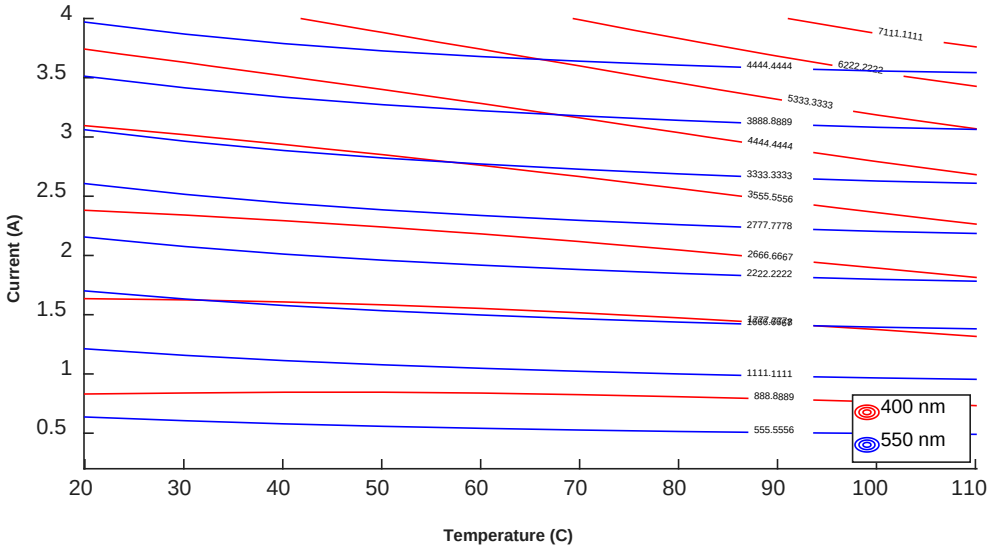
Current (A)
Temperature (C)
400 nm
550 nm
7111.1111
4444.4444
6222.2222
5333.3333
3888.8889
4444.4444
3333.3333
3555.5556
2777.7778
2666.6667
2222.2222
1111.1111
888.8889
555.5556

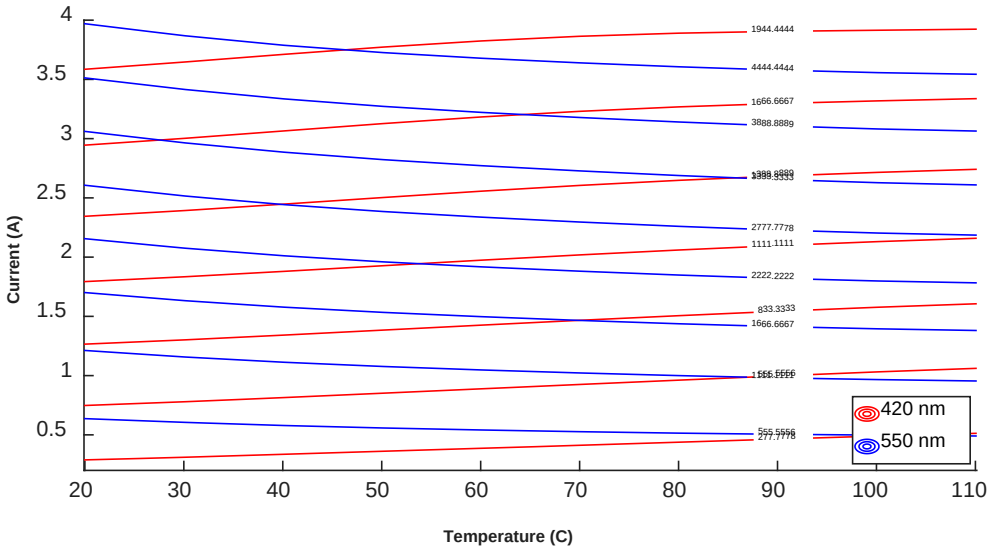
Current (A)
Temperature (C)
420 nm
550 nm
1944.4444
4444.4444
1666.6667
3888.8889
2777.7778
1111.1111
2222.2222
833.3333
1666.6667
277.7778

APPENDIX C. LIGHT EMISSION DATA ANALYSIS CODE

A. MATLAB CALIBRATION CODE

```
% Opens calibration data file and reads data
fid = fopen('370_390_1kHz_0_5_DC_27Aug_05.csv');
tline = fgetl(fid);

% Creates arrays for calibration data to be loaded into
T = [];
I = [];
sens1 = [];
sens2 = [];

% Transfers colums of data from the calibration file to the arrays
while ischar(tline)
   datstr = split(tline,',');
   [dat1,check]=str2num(char(datstr(1)));
   if check
       T = [T str2num(char(datstr(1)))];
       I = [I str2num(char(datstr(2)))];
       sens1 = [sens1 str2num(char(datstr(3)))];
       sens2 = [sens2 str2num(char(datstr(5)))];
   end
   tline = fgetl(fid);
end

sens1 = sens1;
sens2 = sens2;

% Compiles the sensor data into surface matrix based on the current and
temperature
data = [T; I; sens1; sens2]';

testout = sortrows(data);

Imatr = reshape(testout(:,2),length(find(T==min(T))),[]);
Tmatr = reshape(testout(:,1),length(find(T==min(T))),[]);
sens1matr = reshape(testout(:,3),length(find(T==min(T))),[]);
sens2matr = reshape(testout(:,4),length(find(T==min(T))),[]);

% Finds a best-fit polynomial for the sensor surface matrix
p1 = polyfitn([T',I'],sens1',7);
p2 = polyfitn([T',I'],sens2',7);

% Defines the coefficients used for the best-fit polynomials above
sens1sym = polyn2sym(p1);
sens2sym = polyn2sym(p2);

% Converts the coefficients into a format that can be ploted
sens1vec = double(subs(sens1sym));
```

```
sens2vec = double(subs(sens2sym));

sens1fitmatrx = reshape(sens1vec,length(find(T==min(T))),[]);
sens2fitmatrx = reshape(sens2vec,length(find(T==min(T))),[]);

% Ploting the two lock-in output surfaces
figure(1)
ax1 = subplot(1,2,1)
hold on
surf(Tmatr,Imatr,sens1fitmatrx)
plot3(T,I,sens1,'kO', 'MarkerFaceColor', 'r')
grid on
title('420 nm In-Phase Value')                                    %
change
ylabel('\bf\fontsize{18}Current (A)')
xlabel('\bf\fontsize{18}Temperature (C)')
zlabel('\bf\fontsize{18}Sensor Voltage (V)')
axesLabelsAlign3D()
view(45,45)
set(get(gca,'YLabel'),'Rotation',40.0)
set(get(gca,'XLabel'),'Rotation',-40.0)
set(gca,'linewidth',2)
set(gca,'FontSize',20)
ax2 = subplot(1,2,2)
hold on
surf(Tmatr,Imatr,sens2fitmatrx)
plot3(T,I,sens2,'kO', 'MarkerFaceColor', 'r')
grid on
title('550 nm In-Phase Value')
ylabel('\bf\fontsize{18}Current (A)')
xlabel('\bf\fontsize{18}Temperature (C)')
zlabel('\bf\fontsize{18}Sensor Voltage (V)')
set(get(gca,'YLabel'),'Rotation',40.0)
set(get(gca,'XLabel'),'Rotation',-40.0)
set(gca,'linewidth',2)
set(gca,'FontSize',20)
view(45,45)
rotate3d on

% Plots the comparison curves of the surfaces
figure(2)
hold on
levels1 = linspace(0,1000,10); % must be adjusted according to surface
min/max values
[C,h] = contour(Tmatr,Imatr,sens1fitmatrx,levels1,'r-
','DisplayName','420 nm','LineWidth',2);
clabel(C,h,'FontSize',15,'labelspacing',1300)
levels2 = linspace(0,2300,10); % must be adjusted according to surface
min/max values
[C,h] = contour(Tmatr,Imatr,sens2fitmatrx,levels2,'b-
','DisplayName','550 nm','LineWidth',2);
clabel(C,h,'FontSize',15,'labelspacing',1300)
ylabel('\bf\fontsize{28}Current (A)')
xlabel('\bf\fontsize{28}Temperature (C)')
set(gca,'linewidth',2)
```

```
set(gca,'FontSize',36)
legend('420 nm','550 nm','Location','southeast')

% Closed access to the calibration file
fclose(fid);
```

B. SIMULINK LOCK-IN AMPLIFIER AND PREDICTION CODE

1. Lock-In Amplifier Schematic

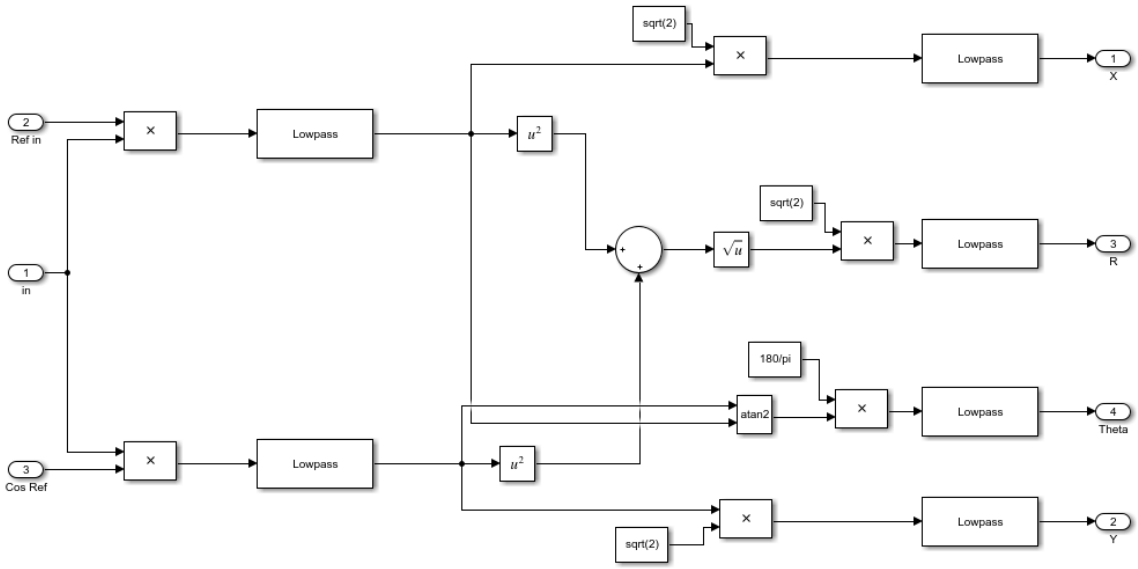

2. Prediction Function Testing Schematic and Code

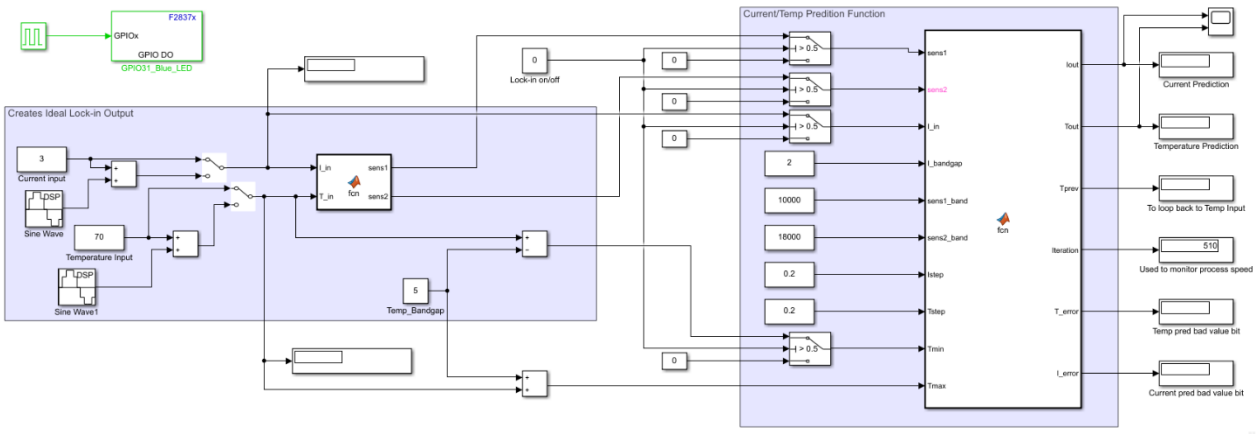

3. Ideal Lock-In Output Function

```
function [sens1,sens2] = fcn(I_in, T_in)
```

```
X1 = I_in;
X2 = T_in;
   % 420 nm calibration polynomials
   sens1 = (1496126078933339*X1^5)/6044629098073145873530088 -
     (155329112974993*X1^4*X2)/1180591620717411303424 +
     (4832022909140803*X1^4)/4722366482869645213696 -
     (2760636205707695*X1^3*X2^2)/1180591620717411303424 +
     (6065822891151987*X1^3*X2)/295147905179352825856 -
     (6783300680161805*X1^3)/18446744073709551616 -
     (2080182060340123*X1^2*X2^3)/18446744073709551616 +
     (4479047787245977*X1^2*X2^2)/9223372036854775808 -
     (7433024235829599*X1^2*X2)/2305843009213693952 +
     (2496827711573073*X1^2)/72057594037927936 -
     (1693876254999409*X1*X2^4)/576460752303423488 +
     (3858991534412331*X1*X2^3)/72057594037927936 -
     (8786880140481683*X1*X2^2)/36028797018963968 +
     (8295362602108313*X1*X2)/9007199254740992 -
     (1742467158771845*X1)/2251799813685248 -
     (1719101211554769*X2^5)/1125899906842624 +
     (8851875138096827*X2^4)/562949953421312 -
     (8291863989589675*X2^3)/140737488355328 +
     (7956886929618135*X2^2)/70368744177664 -
     (392960369699195*X2)/1099511627776 - 7404543670641555/
     281474976710656;
   % 380 nm calibration polynomials
   sens2 = (229503635318333*X1^5)/73786976294838206464 -
      (3367294986519083*X1^4*X2)/18446744073709551616 -
      (7165106123191991*X1^4)/9223372036854775808 +
      (4935043456995805*X1^3*X2^2)/2305843009213693952 +
      (6840369765791837*X1^3*X2)/144115188075855872 +
      (4528004676110721*X1^3)/72057594037927936 -
      (899512580838039*X1^2*X2^3)/18014398509481984 +
      (6052596573669391*X1^2*X2^2)/72057594037927936 -
      (3007497473919997*X1^2*X2)/562949953421312 -
      (6087262055226397*X1^2)/4503599627370496 +
      (8765813992638407*X1*X2^4)/18014398509481984 +
      (2414352146388531*X1*X2^3)/281474976710656 -
      (1171312077160633*X1*X2^2)/17592186044416 +
      (2529688615358733*X1*X2)/8796093022208 -
      (6210793944425371*X1)/140737488355328 +
      (4289773210768927*X2^5)/281474976710656 -
      (5511923451474127*X2^4)/35184372088832 -
      (4937688860082599*X2^3)/35184372088832 +
      (6376953109500443*X2^2)/2199023255552 -
      (4766232204338649*X2)/4398046511104 + 185649726818819/
      137438953472;
```

4. Prediction Solver Function

```
function [Iout,Tout,Tprev,Iteration,T_error,I_error] = fcn(sens1,
sens2, I_in, I_bandgap, sens1_band,sens2_band, Istep, Tstep, Tmin,
Tmax)
```

```
% Tolerance settings
   Ilow = I_in - (0.5 * I_bandgap);
   Imax = I_in + (0.5 *I_bandgap);

   out1low = sens1 - (0.5 * sens1_band);
   out1high = sens1 + (0.5 * sens1_band);


   out2low = sens2 - (0.5 * sens2_band);
   out2high = sens2 + (0.5 * sens2_band);

   Iout = Ilow;
   Tout = Tmin;

% Initial prediction inputs
   X1 = Iout;
   X2 = Tmin;

   pred1 = 0;
   pred2 = 0;

   Iteration = 0;
   I_error = 0;
   T_error = 0;

  while pred1 > out1high && pred2 < out2low && Tout < Tmax
      while pred1 > out1high && X1 < Imax || pred2 < out2low && X1 <
Imax
          Iout = X1;
          X1 = X1 + Istep;
          % 420 nm calibration polynomials
           pred1 = (1496126078933339*X1^5)/60446290980731458735308 8 -
           (155329112974993*X1^4*X2)/1180591620717411303424 +
           (4832022909140803*X1^4)/4722366482869645213696 -
           (2760636205707695*X1^3*X2^2)/1180591620717411303424 +
           (6065822891151987*X1^3*X2)/295147905179352825856 -
           (6783300680161805*X1^3)/18446744073709551616 -
           (2080182060340123*X1^2*X2^3)/18446744073709551616 +
           (4479047787245977*X1^2*X2^2)/9223372036854775808 -
           (7433024235829599*X1^2*X2)/2305843009213693952 +
           (2496827711573073*X1^2)/72057594037927936 -
           (1693876254999409*X1*X2^4)/576460752303423488 +
           (3858991534412331*X1*X2^3)/72057594037927936 -
           (8786880140481683*X1*X2^2)/36028797018963968 +
           (8295362602108313*X1*X2)/9007199254740992 -
           (1742467158771845*X1)/2251799813685248 -
           (1719101211554769*X2^5)/1125899906842624 +
           (8851875138096827*X2^4)/562949953421312 -
           (8291863989589675*X2^3)/140737488355328 +
           (7956886929618135*X2^2)/70368744177664 -
           (392960369699195*X2)/1099511627776 - 7404543670641555/
           281474976710656;

          % 380 nm calibration polynomials
```

```
            pred2 = (229503635318333*X1^5)/73786976294838206464 -
              (3367294986519083*X1^4*X2)/18446744073709551616 -
              (7165106123191991*X1^4)/9223372036854775808 +
              (4935043456995805*X1^3*X2^2)/2305843009213693952 +
              (6840369765791837*X1^3*X2)/144115188075855872 +
              (4528004676110721*X1^3)/72057594037927936 -
              (899512580838039*X1^2*X2^3)/18014398509481984 +
              (6052596573669391*X1^2*X2^2)/72057594037927936 -
              (3007497473919997*X1^2*X2)/562949953421312 -
              (6087262055226397*X1^2)/4503599627370496 +
              (8765813992638407*X1*X2^4)/18014398509481984 +
              (2414352146388531*X1*X2^3)/281474976710656 -
              (1171312077160633*X1*X2^2)/17592186044416 +
              (2529688615358733*X1*X2)/8796093022208 -
              (6210793944425371*X1)/140737488355328 +
              (4289773210768927*X2^5)/281474976710656 -
              (5511923451474127*X2^4)/35184372088832 -
              (4937688860082599*X2^3)/35184372088832 +
              (6376953109500443*X2^2)/2199023255552 -
              (4766232204338649*X2)/4398046511104 + 185649726818819/
              137438953472;
                      Iteration = Iteration + 1;
        end

        if pred1 > out1high || pred2 < out2low
            X2 = X2 + Tstep;
            Tout = Tout + Tstep;

            X1 = Ilow;
            pred1=0;
            pred2=0;
        end

    end
% for future use to limit temp itereations as temp changes
     Tprev = Tout;

% Warning bits that temp or current solution is at edge of tolerance
band
        if Tout >= Tmax - Tstep || Tout <= Tmin + Tstep
            T_error = 1;
        else
            T_error = 0;
        end

        if Iout >= Imax - Istep || Iout <= Ilow + Istep
            I_error = 1;
        else
            I_error = 0;
        End
```

LIST OF REFERENCES

[1] J. A. Russell, “Twenty-first-century innovation pathways for the U.S. Navy in the age of competition,” *Nav. War Coll. Rev.*, vol. 73, no. 3, pp. 1–27, 2020.

[2] A. Aguilar, P. Butler, J. Collins, M. Guerster, B. Kristinsson, P. McKeen, K. Cahoy *et al.*, “Tradespace exploration of the next generation communication satellites,” in AIAA Scitech 2019 Forum, San Diego, California, Jan. 2019. [Online]. doi/10.2514/6.2019-0768

[3] V. K. Khanna, *Fundamentals of Solid-State Lighting: LEDs OLEDs, and Their Applications in Illumination and Displays*, 1st ed. Boca Raton, Florida: CRC Press, USA, 2014.

[4] V. Avrutin, D. Silversmith, Y. Mori, F. Kawamura, Y. Kitaoka, and H. Morkoc, “Growth of bulk GaN and AlN: progress and challenges,” *Proc. IEEE*, vol. 98, no. 7, pp. 1302–1315, 2010.

[5] K. Fujito, S. Kubo, H. Nagaoka, T. Mochizuki, H. Namita, and S. Nagao, “Bulk GaN crystals grown by HVPE,” *J. Cryst. Growth*, vol. 311, no. 10, pp. 3011–3014, May 2009. [Online]. doi: 10.1016/j.jcrysgro.2009.01.046

[6] H. Fujikura, T. Konno, T. Suzuki, T. Kitamura, T. Fujimoto, and T. Yoshida, “Macrodefect-free, large, and thick GaN bulk crystals for high-quality 2–6 in. GaN substrates by hydride vapor phase epitaxy with hardness control,” *Jpn. J. Appl. Phys.*, vol. 57, no. 6, p. 065502, May 2018. [Online]. doi: 10.7567/JJAP.57.065502

[7] R. Dwiliński *et al.*, “Bulk ammonothermal GaN,” *J. Cryst. Growth*, vol. 311, no. 10, pp. 3015–3018, May 2009. [Online]. doi: 10.1016/j.jcrysgro.2009.01.052.

[8] H. Ohta, K. Hayashi, F. Horikiri, M. Yoshino, T. Nakamura, and T. Mishima, “5.0 kV breakdown-voltage vertical GaN p–n junction diodes,” *Jpn. J. Appl. Phys.*, vol. 57, no. 4S, p. 04FG09, Feb. 2018. [Online]. doi: 10.7567/JJAP.57.04FG09

[9] Z. Bian *et al.*, “Leakage mechanism of quasi-vertical GaN Schottky barrier diodes with ultra-low turn-on voltage,” *Appl. Phys. Express*, vol. 12, no. 8, p. 084004, Jul. 2019. [Online]. doi: 10.7567/1882-0786/ab3297

[10] W. Li *et al.*, “Design and realization of GaN trench junction-barrier-schottky-diodes,” *IEEE Trans. Electron Devices*, vol. 64, no. 4, pp. 1635–1641, Apr. 2017. [Online]. doi: 10.1109/TED.2017.2662702

[11] B. J. Baliga, “Power semiconductor device figure of merit for high-frequency applications,” *IEEE Electron Device Lett.*, vol. 10, no. 10, pp. 455–457, Oct. 1989. [Online]. doi: 10.1109/55.43098

[12] R. T. Kemerley, H. B. Wallace, and M. N. Yoder, “Impact of wide bandgap microwave devices on DoD systems,” *Proc. IEEE*, vol. 90, no. 6, pp. 1059–1064, Jun. 2002. [Online]. doi: 10.1109/JPROC.2002.1021570

[13] A. Tosi, A. D. Mora, F. Pozzi, and F. Zappa, “Modeling and probing hot-carrier luminescence from MOSFETs,” *IEEE Electron Device Lett.*, vol. 29, no. 4, pp. 350–352, 2008.

[14] S. M. Khanna, A. Houdayer, A. Jorio, C. Carlone, M. Parentean, and J. W. Gerdes, “Nuclear radiation displacement damage prediction in Gallium Arsenide through low temperature photoluminescence measurements,” *IEEE Trans. Nucl. Sci.*, vol. 43, no. 6, pp. 2601–2608, 1996.

[15] L. Ceccarelli, H. Luo, and F. Iannuzzo, “Investigating SiC MOSFET body diode’s light emission as temperature-sensitive electrical parameter,” *Microelectron. Reliab.*, pp. 627–630, 2018.

[16] S. Kalker, C. H. van der Broeck, and R. W. De Doncker, “Utilizing Eelectroluminescence of SiC MOSFETs for unified junction-temperature and current sensing,” in *2020 IEEE Applied Power Electronics Conference and Exposition (APEC)*, Mar. 2020, pp. 1098–1105. [Online]. doi: 10.1109/APEC39645.2020.9124517

[17] J. Winkler, J. Homoth, H. Bartolf, and I. Kallfass, “Study on transient light emission of SiC power MOSFETs regarding the sensing of source-drain currents in hard-switched power electronic applications,” in *PCIM Europe 2019; International Exhibition and Conference for Power Electronics, Intelligent Motion, Renewable Energy and Energy Management*, May 2019, pp. 1–8.

[18] J. Winkler, J. Homoth, and I. Kallfass, “Electroluminescence-based junction temperature measurement approach for SiC power MOSFETs,” *IEEE Trans. Power Electron.*, vol. 35, no. 3, pp. 2990–2998, 2020, doi: 10.1109/tpel.2019.2929426

[19] M. Broeg, “Current and temperature sensing via light emission from bulk GaN PN junctions,” M.S. thesis, Dept. of Elec. Eng., NPS, Monterey, USA. 2019.

[20] G. Gunn, *Critical Metals Handbook*. Hoboken, NJ: John Wiley & Sons, USA, 2014.

[21] J. L. Hudgins, G. S. Simin, E. Santi, and M. A. Khan, “An assessment of wide bandgap semiconductors for power devices,” *IEEE Trans. Power Electron.*, vol. 18, no. 3, pp. 907–914, May 2003. [Online]. doi: 10.1109/TPEL.2003.810840

[22] B. J. Baliga, *Fundamentals of Power Semiconductor Devices*, 1st ed. 2008. New York, NY, USA: Springer US, 2008.

[23] J. Millán, P. Godignon, X. Perpiñà, A. Pérez-Tomás, and J. Rebollo, "A Survey of Wide Bandgap Power Semiconductor Devices," *IEEE Trans. Power Electron.*, vol. 29, no. 5, pp. 2155–2163, May 2014. [Online]. doi: 10.1109/TPEL.2013.2268900.

[24] M. Alam, "ECE 606 Lecture 13: Recombination-Generation," *Nanohub by Purdue University*, Feb. 15, 2009. [Online]. https://nanohub.org/resources/5807

[25] M. A. Porter, J. Williams, M. Broeg, K. Corzine, and T. Weatherford, "Current and temperature measurement via spectral decomposition of light emission from a GaN power diode," in *2020 IEEE Applied Power Electronics Conference and Exposition (APEC)*, Mar. 2020, pp. 640–646. [Online]. doi: 10.1109/APEC39645.2020.9124317.

[26] N. Mohan, *Power electronics: converters, applications, and design*, 3rd ed. Place of publication not identified. New York, USA: John Wiley & Sons, 2003.

[27] R. Mammano, "Switching power supply topology voltage mode vs. current mode." Unitrode, 1999, [Online]. Available: https://www.ti.com/lit/an/slua119/slua119.pdf?ts=1603393180769&ref_url=https%253A%252F%252Fwww.google.com%252F

[28] Y. Wang, J.-G. Liu, J. Zhao, and Y. Yang, "Split core closed loop hall effect current sensors and applications," Nuremburg, Germany, May 2012, pp. 1633–1638.

[29] O. Aiello, P. Crovetti, and F. Fiori, "Investigation on the susceptibility of hall-effect current sensors to EMI," in *10th International Symposium on Electromagnetic Compatibility*, Sep. 2011, pp. 368–372.

[30] M. Krupa and M. Gasior, "A precise pulsed current source for absolute calibration of current measurement systems with no DC response," *Int. Beam Instrum. Conf.*, pp. 165–168, 2016.

[31] "SRS tech note." Stanford Research Systems, Apr. 07, 2020, [Online]. Available: https://www.thinksrs.com/downloads/pdfs/applicationnotes/Lock-In%20Basics.pdf

[32] I. Gautam, *An introduction to Texas Instruments C2000 Realtime Control Microcontrollers*. Independently published, 2017.

[33] Texas Instruments, “TMS320F2837xD duel-core microcontrollers datasheet.” Texas Instruments, [Online]. Available: https://www.ti.com/lit/ds/sprs880m/sprs880m.pdf?ts=1599525797074&ref_url=https%253A%252F%252Fwww.ti.com%252Ftool%252FLAUNCHXL-F28379D

INITIAL DISTRIBUTION LIST

1. Defense Technical Information Center
   Ft. Belvoir, Virginia

2. Dudley Knox Library
   Naval Postgraduate School
   Monterey, California